



Defense Threat Reduction Agency
8725 John J. Kingman Road, MS
6201 Fort Belvoir, VA 22060-6201



DTRA-TR-16-9

TECHNICAL REPORT

Radiation-Hard and Self-Healing Substrate-Agnostic Nanocrystalline ZnO Thin Film Electronics (Per5-E)

Distribution Statement A. Approved for public release; distribution is unlimited.

June 2017

11-2335M

Gregg Jessen and
Tom Jackson

Prepared by:
AFRL/Rydd
2241 Avionics Circle
WPAFB, OH 45433

DESTRUCTION NOTICE:

Destroy this report when it is no longer needed.
Do not return to sender.

PLEASE NOTIFY THE DEFENSE THREAT REDUCTION
AGENCY, ATTN: DTRIAC/ J9STT, 8725 JOHN J. KINGMAN ROAD,
MS-6201, FT BELVOIR, VA 22060-6201, IF YOUR ADDRESS
IS INCORRECT, IF YOU WISH IT DELETED FROM THE
DISTRIBUTION LIST, OR IF THE ADDRESSEE IS NO
LONGER EMPLOYED BY YOUR ORGANIZATION.

REPORT DOCUMENTATION PAGE				<i>Form Approved</i> OMB No. 0704-0188	
Public reporting burden for this collection of information is estimated to average 1 hour per response, including the time for reviewing instructions, searching existing data sources, gathering and maintaining the data needed, and completing and reviewing this collection of information. Send comments regarding this burden estimate or any other aspect of this collection of information, including suggestions for reducing this burden to Department of Defense, Washington Headquarters Services, Directorate for Information Operations and Reports (0704-0188), 1215 Jefferson Davis Highway, Suite 1204, Arlington, VA 22202-4302. Respondents should be aware that notwithstanding any other provision of law, no person shall be subject to any penalty for failing to comply with a collection of information if it does not display a currently valid OMB control number. PLEASE DO NOT RETURN YOUR FORM TO THE ABOVE ADDRESS.					
1. REPORT DATE (DD-MM-YYYY) 00-06-2017		2. REPORT TYPE Technical		3. DATES COVERED (From - To) October 1, 2011 - January 8, 2015	
4. TITLE AND SUBTITLE Radiation-Hard and Self-Healing Substrate-Agnostic Nanocrystalline ZnO Thin Film Electronics (Per5-E)				5a. CONTRACT NUMBER 11-2335M	
				5b. GRANT NUMBER	
				5c. PROGRAM ELEMENT NUMBER 0601000BR	
6. AUTHOR(S) Gregg Jessen, AFRL Tom Jackson, PSU				5d. PROJECT NUMBER	
				5e. TASK NUMBER	
				5f. WORK UNIT NUMBER	
7. PERFORMING ORGANIZATION NAME(S) AND ADDRESS(ES) AFRL/Rydd, 2241 Avionics Circle, WPAFB, OH 45433 Penn State University, 480 Old Main, University Park, PA, 16802				8. PERFORMING ORGANIZATION REPORT NUMBER	
9. SPONSORING / MONITORING AGENCY NAME(S) AND ADDRESS(ES) Defense Threat Reduction Agency 8725 John J. Kingman Road, STOP 6201 Fort Belvoir, VA 22060-6201				10. SPONSOR/MONITOR'S ACRONYM(S) DTRA	
				11. SPONSOR/MONITOR'S REPORT NUMBER(S) DTRA-TR-16-9	
12. DISTRIBUTION / AVAILABILITY STATEMENT Distribution Statement A. Approved for public release; distribution is unlimited.					
13. SUPPLEMENTARY NOTES PROPOSAL#: BRCALL08-Per5-E-2-0021; PERF. CODE: AFHEST MIPR#s: -2335M; HDTRA124564					
14. ABSTRACT The objective of the effort was to advance the fundamental understanding of radiation induced changes in the electronic properties of metal-oxide (M-O) semiconductors with s-orbital dominated conduction bands because of their potential for radiation hardness and self-healing very different (and potentially better) than sp-hybrid bonded semiconductors. The effort has produced models based on experimental results regarding radiation-induced changes in wide bandgap ZnO films and devices. A combination of material deposition techniques and radiation induced changes on films with varied microstructures were studied.					
15. SUBJECT TERMS ZnO, TFT, radiation hard, self-healing					
16. SECURITY CLASSIFICATION OF:			17. LIMITATION OF ABSTRACT SAR	18. NUMBER OF PAGES 69	19a. NAME OF RESPONSIBLE PERSON Jacob Calkins
a. REPORT Unclassified	b. ABSTRACT Unclassified	c. THIS PAGE Unclassified			19b. TELEPHONE NUMBER (include area code) 703-767-3075

UNIT CONVERSION TABLE

U.S. customary units to and from international units of measurement^{*}

U.S. Customary Units	<div style="display: inline-block; text-align: right;"> Multiply by </div> <div style="display: inline-block; text-align: left;"> Divide by[†] </div>	International Units
Length/Area/Volume		
inch (in)	2.54 $\times 10^{-2}$	meter (m)
foot (ft)	3.048 $\times 10^{-1}$	meter (m)
yard (yd)	9.144 $\times 10^{-1}$	meter (m)
mile (mi, international)	1.609 344 $\times 10^3$	meter (m)
mile (nmi, nautical, U.S.)	1.852 $\times 10^3$	meter (m)
barn (b)	1 $\times 10^{-28}$	square meter (m ²)
gallon (gal, U.S. liquid)	3.785 412 $\times 10^{-3}$	cubic meter (m ³)
cubic foot (ft ³)	2.831 685 $\times 10^{-2}$	cubic meter (m ³)
Mass/Density		
pound (lb)	4.535 924 $\times 10^{-1}$	kilogram (kg)
unified atomic mass unit (amu)	1.660 539 $\times 10^{-27}$	kilogram (kg)
pound-mass per cubic foot (lb ft ⁻³)	1.601 846 $\times 10^1$	kilogram per cubic meter (kg m ⁻³)
pound-force (lbf avoirdupois)	4.448 222	newton (N)
Energy/Work/Power		
electron volt (eV)	1.602 177 $\times 10^{-19}$	joule (J)
erg	1 $\times 10^{-7}$	joule (J)
kiloton (kt) (TNT equivalent)	4.184 $\times 10^{12}$	joule (J)
British thermal unit (Btu) (thermochemical)	1.054 350 $\times 10^3$	joule (J)
foot-pound-force (ft lbf)	1.355 818	joule (J)
calorie (cal) (thermochemical)	4.184	joule (J)
Pressure		
atmosphere (atm)	1.013 250 $\times 10^5$	pascal (Pa)
pound force per square inch (psi)	6.984 757 $\times 10^3$	pascal (Pa)
Temperature		
degree Fahrenheit (°F)	[T(°F) – 32]/1.8	degree Celsius (°C)
degree Fahrenheit (°F)	[T(°F) + 459.67]/1.8	kelvin (K)
Radiation		
curie (Ci) [activity of radionuclides]	3.7 $\times 10^{10}$	per second (s ⁻¹) [becquerel (Bq)]
roentgen (R) [air exposure]	2.579 760 $\times 10^{-4}$	coulomb per kilogram (C kg ⁻¹)
rad [absorbed dose]	1 $\times 10^{-2}$	joule per kilogram (J kg ⁻¹) [gray (Gy)]
rem [equivalent and effective dose]	1 $\times 10^{-2}$	joule per kilogram (J kg ⁻¹) [sievert (Sv)]

^{*} Specific details regarding the implementation of SI units may be viewed at <http://www.bipm.org/en/si/>.

[†] Multiply the U.S. customary unit by the factor to get the international unit. Divide the international unit by the factor to get the U.S. customary unit.

Grant/Award #: 11-2335M

PI Name: Gregg Jessen, **Co-PI:** Tom Jackson

Organization/Institution: Air Force Research Laboratory, **Co-PI:** Penn State University

Project Title: Radiation-Hard and Self-Healing Substrate-Agnostic Nanocrystalline ZnO Thin Film Electronics (Per5-E)

Final Report

Year #1 Period of Performance: June 2011 – June 2012

Year #2 Period of Performance: July 2012 – June 2013

Year #3 Current and Final Reporting Period: July 2013 – September 2014

What are the major goals of the project?

List the major goals of the project as stated in the approved application or as approved by the agency. If the application lists milestones/target dates for important activities or phases of the project, identify these dates and show actual completion dates or the percentage of completion. Generally, the goals will not change from one reporting period to the next. However, if the awarding agency approved changes to the goals during the reporting period, list the revised goals and objectives. Also explain any significant changes in approach or methods from the agency approved application or plan.

The goals for this research are found in the original proposal BRCALL08-Per5-E-2-0021.

“The objective of the proposed project is to advance the fundamental understanding of radiation induced changes in the electronic properties of metal-oxide (M-O) semiconductors with s-orbital dominated conduction bands. s-orbital conduction band materials are particularly interesting because they offer potential for radiation hardness and self-healing very different (and potentially better) than sp-hybrid bonded semiconductors. Although radiation hardness for silicon and III-V bulk semiconductor devices has been extensively studied, much less is known about radiation-induced effects on wide bandgap thin-film transistors. The proposed work will provide models based on experimental results regarding radiation-induced changes in wide bandgap ZnO films and devices. Using a combination of material deposition techniques, radiation induced changes on films with varied microstructures will be studied. Both simple films and realistic device structures, including combinations of ZnO thin films and high-k dielectrics, will be studied. The scientific knowledge gained by this work will allow the design and fabrication of radiation hard, substrate-agnostic electronic circuits that can be easily integrated with other circuits.”

Prior to the program, preliminary data suggested that metal-oxide TFTs should be robust in the presence of ionizing radiation as shown in Figure 1. In the first year, the goals of this program were to assess the state of the art in thin-film transistor radiation hardness and compare with metal-oxide TFT technology. As a test case, the work was to begin with ZnO TFTs produced by two different techniques, PLD and PEALD, and develop transistor models addressing the radiation induced changes in device performance.

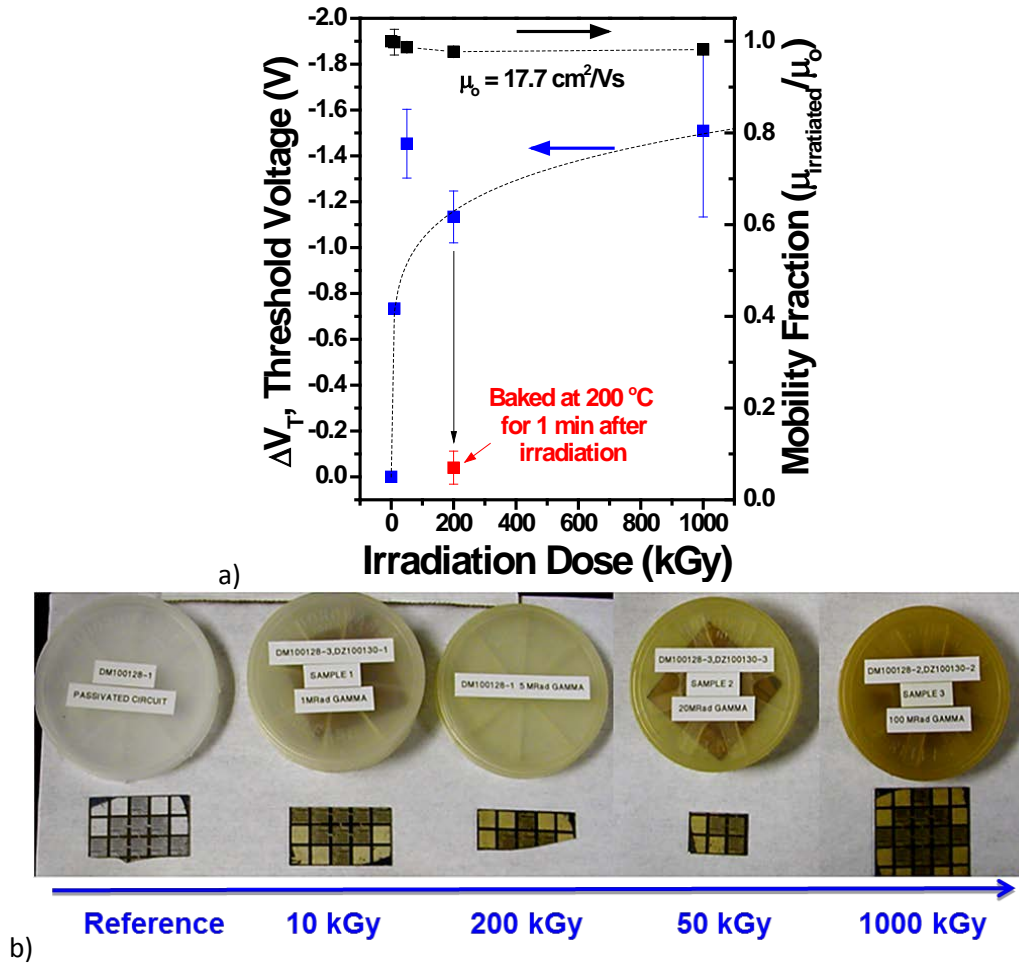


Figure 1. a) Early results indicating small shifts in threshold voltage and virtually no change in mobility as a function of ^{60}Co gamma ray exposure. Dramatic recovery was observed after a short post-irradiation bake in air at 200 °C for 1 minute. b) Color centers formed in samples and carrier shown for reference as a function of dose.

In the second year, designs of experiments were planned to study the influence of material growth, device design and passivation parameters on radiation sensitivity and self-healing characteristics and provide data to develop physical device modeling for ZnO TFTs. During this period, AFRL appropriated civilian positions were 100% funded and we requested reprogramming of DTRA funds to increase the level of spectroscopic material characterization with the goal of using this data to improve the device modeling efforts.

In the third year, the goal was to progress to advanced metal-oxide material development and continue fabrication and radiation testing of advanced device structures. However, in the second year, we found the need to continue investigation of the standard ZnO TFT structures with simple interfaces to isolate the location of the radiation impacts. The goals of radiation testing, analysis and modeling remained the same, but were carried out on the standard devices with experiments designed to isolate the physical location of the interfaces affected by radiation induced changes.

The following tasks were proposed as goals during the program and are now complete.

Year 1

Task 1: Comprehensive literature survey

Task 2: Rad-hard assessment of the current ZnO TFT designs

Task 3: Initial radiation sensitivity modeling

Task 4: Annual report

Year 2

Task 5: Design of Experiments

Task 6: Characterization, radiation tests and analysis

Task 7: Physical device modeling

Task 8: Annual report

Year 3

Task 9¹: Advanced M-O Material Development

Task 10¹: Fabrication, characterization, radiation tests and analysis of advanced devices

Task 11¹: Modeling of advanced devices

Task 12: Final report

¹ These tasks were modified to focus on standard device materials based on ZnO in order to isolate the physical location of radiation induced effects.

What was accomplished under these goals?

For this reporting period describe: 1) major activities; 2) specific objectives; 3) significant results, including major findings, developments, or conclusions (both positive and negative); and 4) key outcomes or other achievements. Include a discussion of stated goals not met. As the project progresses, the emphasis in reporting in this section should shift from reporting activities to reporting accomplishments.

In this section, a list of the major activities is reported for each task. The objectives, results, and outcomes are reported within each major activity.

The major accomplishments fall under the following categories:

- 1. Literature Survey**
- 2. Materials and Device Fabrication**
- 3. Electrical Characterization of Irradiated Devices and Development of In-Situ measurement Techniques**
- 4. Materials Characterization and Defect Analysis**
- 5. Device Modeling**

Literature Survey

A comprehensive literature survey was started at the beginning of the program and key seminal works were studied to compare with current state-of-the-art thin film technology. These works were continually used as fiduciaries during the course of the project. This task continued for the remainder of the project. The primary references used during the first year can be found in [1] – [42]. The main topics surveyed can be summarized as:

- 1) Characterization of radiation effects in CMOS or silicon devices and circuits
- 2) Characterization of radiation effects in TFTs, both covalent and ionic bond materials

The literature survey set the tone for future research direction in terms of establishing figures of merit for measurement and characterization of radiation effects. Radiation effects have been well assessed in single-crystal silicon CMOS technology, amorphous-silicon and poly-crystalline silicon TFTs. Devices have been characterized as a function of radiation dose both biased and unbiased during irradiation. A comparison of turn-on voltage (V_{ON}) for varying technologies from the literature can be found in Figure 2 as a function of dose. In this case, V_{ON} is defined as the gate-source bias resulting in drain current of 0.1 nA. The literature shows that V_{ON} changes rapidly at low irradiation doses for the technologies surveyed. For comparison, our early work is included in this figure showing the relatively high radiation tolerance of ZnO TFTs to radiation exposure.

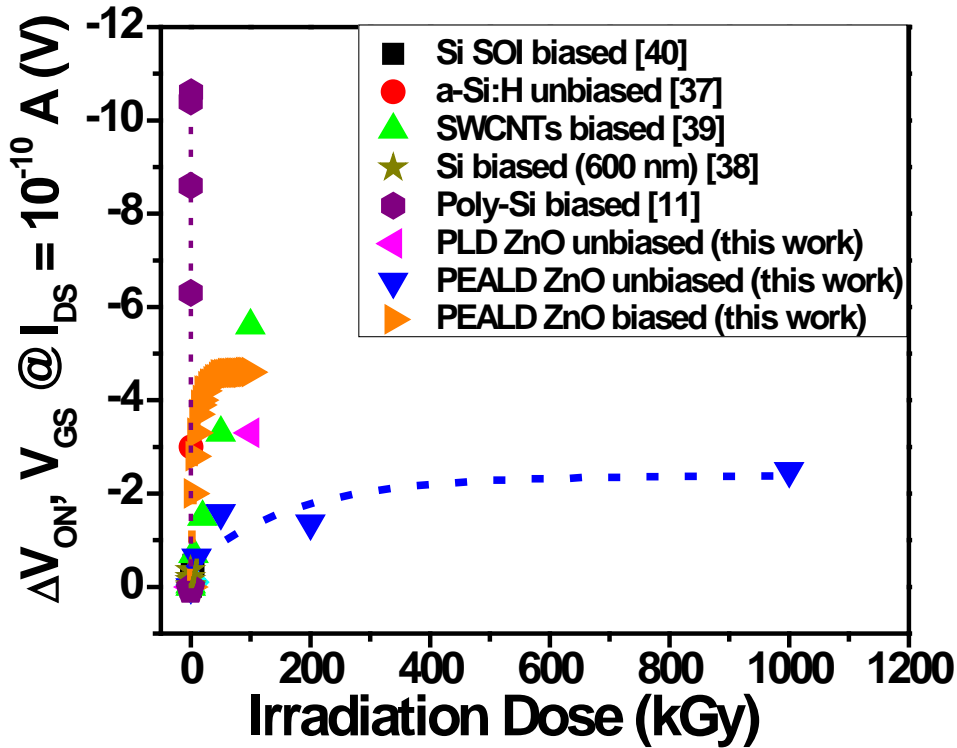


Figure 2. Comparison of V_{ON} shift for biased and unbiased devices with literature results as a function of dose. There is substantial variation for different technologies. However, ZnO TFTs fabricated in this program exhibit significantly better radiation tolerance than other Si or C based thin-film devices.

There are also numerous reports on passivation strategies of ZnO-based TFTs suggesting the importance of passivation material selection. As an example, Figure 3 shows an experiment by Nomura et al [43] on the effects of passivation variation for amorphous In-Ga-Zn-O (a-IGZO) TFTs. The transfer curves show that devices are well passivated for some films such as Y_2O_3 or Al_2O_3 but are conducting with films such as SiO_2 or HfO_2 . Due to the large variation in device performance, it was critical for this project to compare, contrast and select a passivation method that is electrically stable for the irradiation experiments so that radiation effects and passivation effects are easily distinguished.

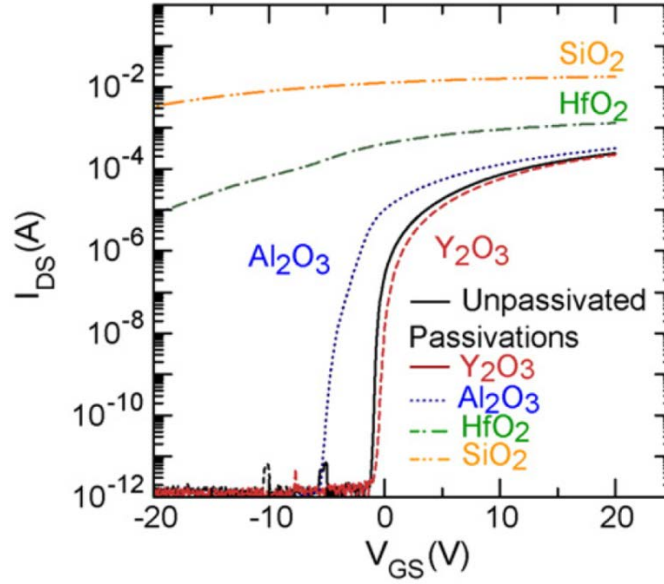


Figure 3. Transfer curves for a-IGZO TFTs as a function of passivation taken from Nomura et al [43].

Materials and Device Fabrication

During the first year effort, an assessment was completed for ZnO TFT designs. These designs include permutations in the active, dielectric, and passivation layers of the device. ZnO active layers have been grown by pulsed-laser deposition (PLD) and plasma-enhanced atomic layer deposition (PEALD). Gate dielectrics deposited by plasma-enhanced chemical vapor deposition (PECVD) and PEALD have been compared. Finally, several types of passivation have been compared including films deposited by PECVD and atomic layer deposition (ALD). Figure 4 depicts a layout for a typical bottom-gated TFT and a cross-section SEM image of a ZnO layer deposited on top of a SiO₂ dielectric with a Ni/Au gate metal. Though PLD and PEALD growth techniques are vastly different, the resulting film characteristics are remarkably consistent with grain sizes ranging from 10 – 50 nm and RMS roughness < 2 nm.

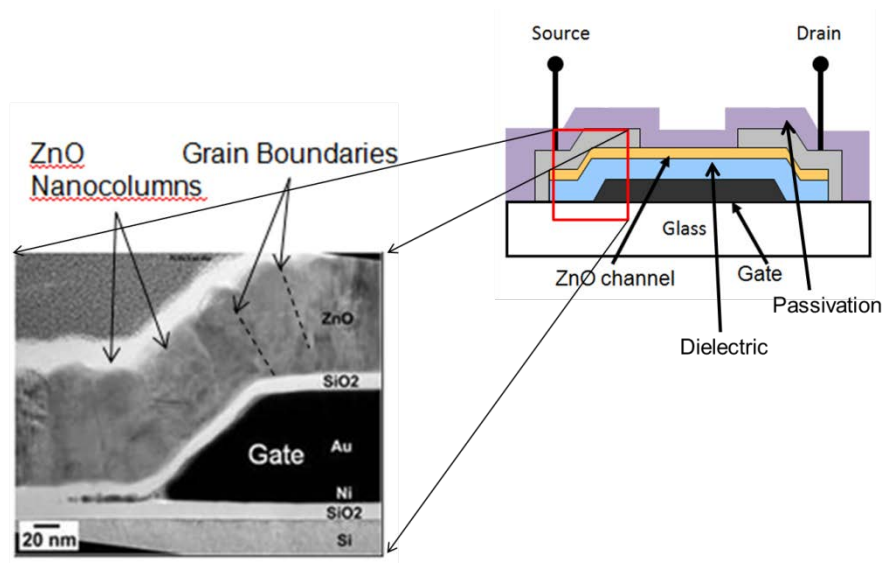


Figure 4. Cross-sectional view of typical TFT layout. The left side shows an SEM image of a device at the source edge of the gate. The right side shows a completed device.

In order to establish a baseline structure for subsequent experiments, several variations of device structures with differing passivation schemes were characterized for stability and initial irradiation effects. Devices with 50 nm PLD ZnO active layers are compared with devices with 10 nm PEALD ZnO active layers. For clarification of layers varied in the device structure, see Figure 4. Device schemes with the following layer stacks have been investigated (listed in order of deposition as gate-dielectric/ZnO type/**passivation**):

Device schemes with the following layer stacks have been investigated (listed in order of deposition as gate-dielectric/ZnO type/**passivation**):

1. PECVD SiO₂/PLD ZnO/**unpassivated**
2. PECVD SiO₂/PLD ZnO/**PECVD SiO₂**
3. PECVD SiO₂/PLD ZnO/**ALD Al₂O₃**
4. PECVD SiO₂/PLD ZnO/**PEALD Al₂O₃**
5. HfO₂/PLD ZnO/**unpassivated**
6. HfO₂/PLD ZnO/**polyimide**
7. HfO₂/PLD ZnO/**ALD Al₂O₃**
8. HfO₂/PLD ZnO/**PEALD Al₂O₃**
9. Al₂O₃/PEALD ZnO/**ALD Al₂O₃**
10. Al₂O₃/PEALD ZnO/**PEALD Al₂O₃**
11. Al₂O₃/PEALD ZnO/**PECVD SiO₂**

PLD ZnO TFTs passivated with PECVD SiO₂ exhibited the best electrical performance as in structure #2. The transfer characteristics are very stable with no shift in V_T or change in mobility values. Representative data from different devices overlap in both passivated and unpassivated cases. Generally, PECVD SiO₂ passivation does not change device performance of PLD grown ZnO TFTs. However, samples exposed to 10 Mrad of gamma radiation become conductive and do not pinch off. These devices do not recover their pre-irradiation characteristics even after annealing at 200 °C. This could indicate damage or the formation of a channel at the ZnO/passivation interface. Figure 5 shows transfer characteristics for PLD devices with passivation and without as well as the impact of gamma radiation exposure on PECVD SiO₂ passivated TFTs. PLD devices with PECVD SiO₂ passivation were not used in further experiments. However, the effect of passivation was studied later in the program.

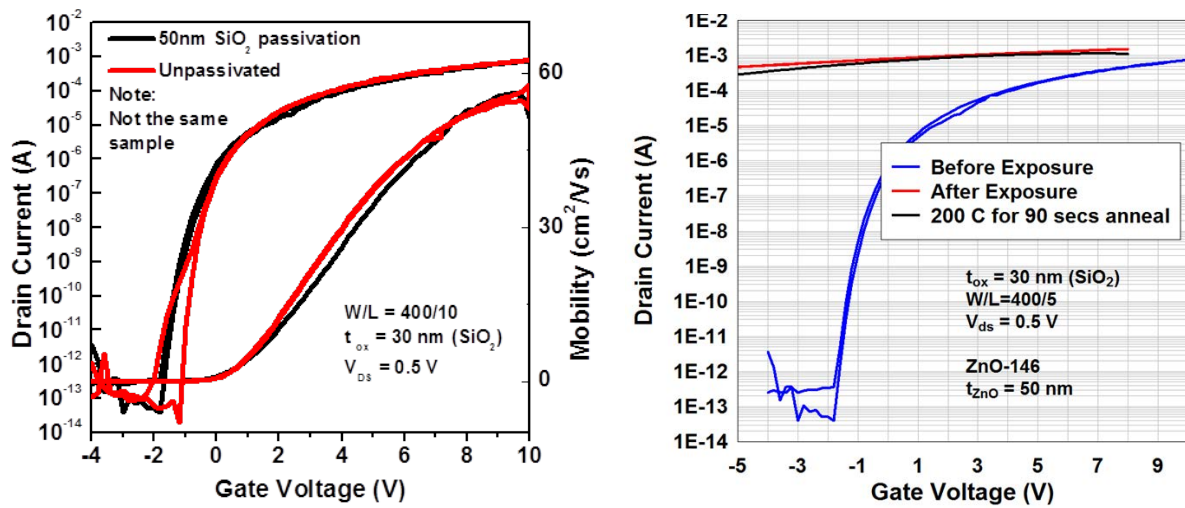


Figure 5. Left: Transfer characteristics for representative PLD ZnO TFTs comparing PECVD SiO₂ passivated devices to unpassivated devices. Right: PLD ZnO TFTs with PECVD SiO₂ passivation exposed to 10 Mrad gamma radiation and annealed.

Further studies on PLD ZnO TFTs passivated by ALD and PEALD Al_2O_3 show conduction at the ZnO/passivation interface even without irradiation. This is true for all layer stacks using PLD ZnO with both PECVD SiO_2 and HfO_2 gate dielectrics as in stacks #3, #4, #7, and #8. Figure 6 shows transfer characteristics for Al_2O_3 passivated PLD ZnO TFTs. The ability to modulate the channel is completely lost. This indicates process induced damage or the formation of a channel at the interface that cannot be pinched off due to the thicker PLD ZnO layer.

Any passivation schemes involving the HfO_2 dielectric under PLD ZnO films (as in #5, #6, #7, and #8) were unstable and were down-selected because instability prevented us from having meaningful radiation-induced results. The polyimide passivation experiment was inconclusive due to the instability from the HfO_2 dielectric. However, we do not anticipate polyimide to be robust to irradiation. So polyimide passivation layer was also down-selected.

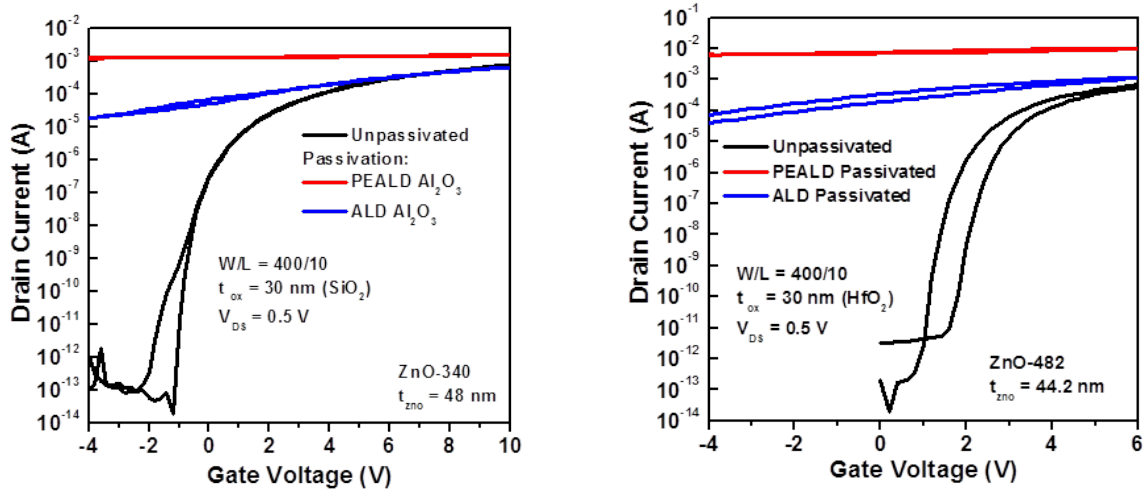


Figure 6. Transfer characteristics of PLD ZnO TFTs before and after passivation with ALD and PEALD Al_2O_3 . On the left are results from TFTs with PECVD SiO_2 gate dielectric. On the right are results from TFTs with HfO_2 gate dielectric. In all cases, the ability to modulate the channel is lost.

PEALD ZnO TFTs show different behavior. Aside from the growth technique, the major difference between these devices and PLD ZnO devices is the relatively thin, 10nm ZnO layer. For PEALD ZnO TFTs, all types of passivation resulted in devices that could modulate except for PEALD Al_2O_3 . However, every device exhibited some negative V_{ON} shift after passivation. This indicates leakage at the PEALD ZnO/passivation interface that can be pinched off due to closer proximity to the gate. Figure 7 shows transfer characteristics for PEALD ZnO TFTs with passivation. ALD Al_2O_3 passivation results in a V_{ON} shift of -2.0 – -3.2 V, PECVD SiO_2 passivation results in a V_{T} shift of about -3.0 V, and PEALD Al_2O_3 passivation results in conduction.

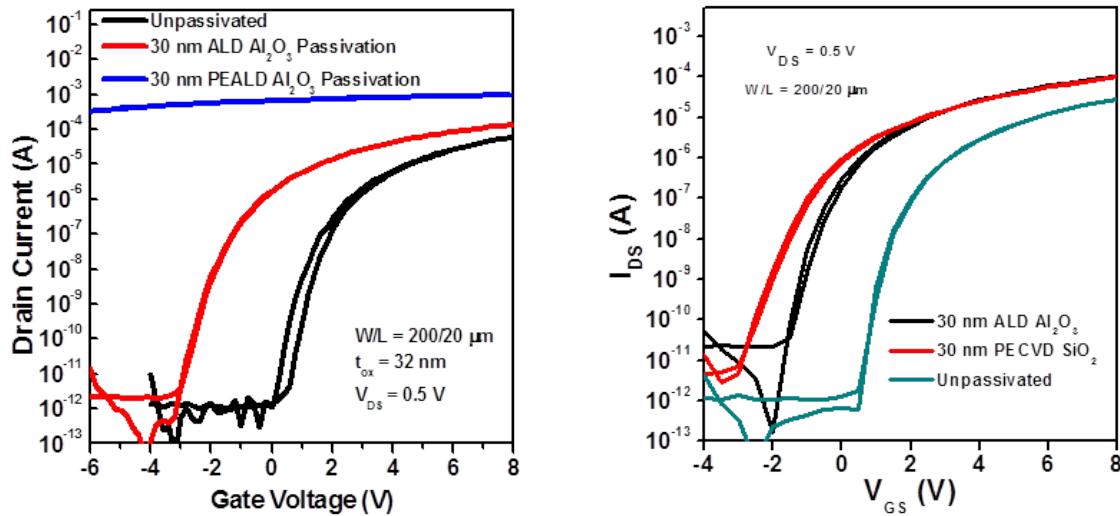


Figure 7. Transfer characteristics for PEALD ZnO TFTs passivated with ALD Al_2O_3 and PEALD Al_2O_3 (left side) and PEALD ZnO TFTs passivated with ALD Al_2O_3 and PECVD SiO_2 (right side). PEALD Al_2O_3 passivation results in loss of channel control.

Variation studies in gate dielectric and passivation layers were completed including SiO_2 , Al_2O_3 , HfO_2 , and polyimide. Significant changes were seen in device performance, leakage currents, and turn-on voltage shifts due to these variations. As a result, the number of permutations in epitaxial layers and gate dielectrics has been reduced to 2 main types: 1) PECVD SiO_2 gate dielectric with PLD ZnO active layer and 2) PEALD Al_2O_3 gate dielectric with PEALD ZnO active layer. Even though the physical growth mechanisms of each technique are different, they show similarities in nanocrystalline size, crystal orientation, and electrical performance. A comparison between ZnO materials grown by different techniques allows more general conclusions to be drawn regarding radiation effects in ZnO materials, while the smaller number of layer permutations reduces the chance that radiation effects are masked by effects of device fabrication.

Sample and Process Exchange

The objective of this activity was to compare and contrast sample variations as a function of epitaxial growth, semiconductor/dielectric interface, and passivation deposited by different techniques. Round-robin experiments were compared to the baseline AFRL and PSU processes. There are two round-robin experiments (RR1 and RR2).

Figure 8 shows a schematic cross-section of the baseline structures. The nominal AFRL process flow is a p-Si substrate-gated device with a PECVD SiO₂ gate dielectric and PLD ZnO active layer. The nominal PSU process flow is a metal gated device with a PEALD Al₂O₃ gate dielectric and PEALD ZnO active layer. The baseline device structures are listed below.

- 1) PEALD Al₂O₃ – 30 nm/ PEALD ZnO 10 nm (baseline PSU structure)
- 2) PECVD SiO₂ – 25 nm/ PLD ZnO 50 nm (baseline AFRL structure)

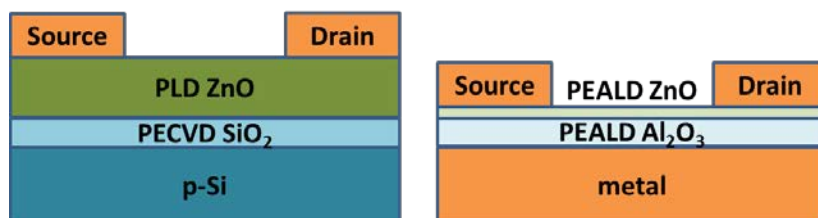


Figure 8. Baseline AFRL structure on the left where the p-Si gate is the substrate. The baseline PSU structure is shown on the right and the substrate is omitted for clarity.

The RR1 experiment involved a gate-dielectric swap from the baseline structures in which the baseline PEALD gate-dielectric from PSU was deposited on AFRL substrates which were returned to AFRL for PLD ZnO deposition and then the baseline PECVD gate-dielectric from AFRL was deposited on PSU substrates which were returned to PSU for PEALD ZnO deposition. Both samples were passivated by ALD Al₂O₃. The resulting layer stacks are shown in Figure 9. The modified baseline structures are listed below.

- 3) PECVD SiO₂ – 25 nm / PEALD ZnO – 10nm/ ALD Al₂O₃ – 32 nm
- 4) PEALD Al₂O₃ – 30 nm/ PLD ZnO – 50nm/ ALD Al₂O₃ – 32 nm

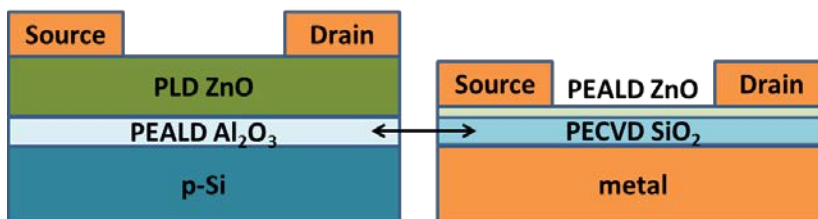


Figure 9. First round-robin experiment where the gate dielectric in the baseline structures were swapped.

A summary of the transfer characteristics comparison is shown in Figure 10 for both unpassivated and passivated devices. On the left are devices with PEALD ZnO films grown on both PECVD SiO₂ and PEALD Al₂O₃ gate dielectrics. On the right are devices with PLD ZnO films grown on both PECVD SiO₂ and PEALD Al₂O₃ gate dielectrics. Both types of devices were then passivated with ALD Al₂O₃.

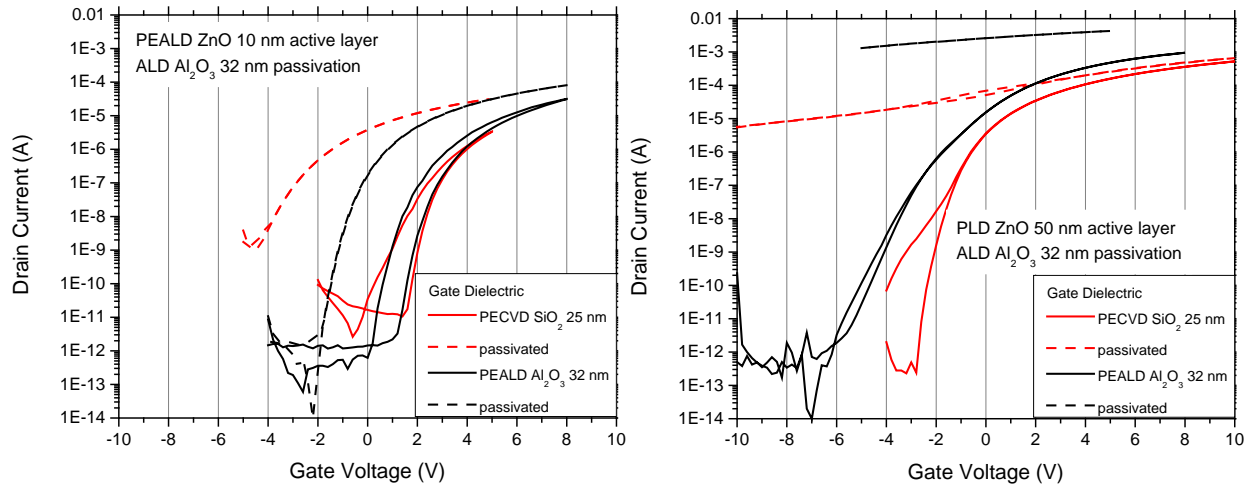


Figure 10 Transfer characteristics of unpassivated and passivated TFTs for ZnO layers grown on both PEALD Al_2O_3 and PECVD SiO_2 gate-dielectrics from RR1 as compared to the baseline structures. ZnO thin films grown by PEALD are shown on the left and ZnO films grown by PLD are shown on the right.

Before passivation, the characteristics for the PEALD ZnO and PLD ZnO devices on both PECVD SiO_2 and PEALD Al_2O_3 gate dielectrics are generally similar. Although hysteresis in the subthreshold region complicates analysis, the PEALD ZnO devices have threshold voltage near 3 V, the PLD ZnO devices have threshold voltage near 0 V.

After passivation, the results are quite different. For the PEALD ZnO devices the device characteristics shift negative. To avoid complications from the hysteresis in the subthreshold region, we estimated the shift from the high current portion of the device curves. For the PEALD ZnO device with Al_2O_3 gate dielectric the shift is about -2.7 V, for the PEALD ZnO device with SiO_2 gate dielectric the shift is about -5.2 V. Using a model of passivation induced charge at the ZnO back surface [44] the shift would be expected to scale with the combination of gate dielectric and active layer capacitance. The shift for SiO_2 compared to Al_2O_3 (and taking into account the thicknesses) is somewhat larger than this simple model would predict.

The after passivation results for the PLD ZnO devices are somewhat different. The PLD ZnO device with SiO_2 gate dielectric is somewhat similar to the PEALD devices. Considering only the high current portion of the characteristics the device shows a shift of about -1.8 V. The change in subthreshold characteristics is more dramatic. This is not completely unexpected. Because the ZnO thickness for the PLD devices is thicker than for the PEALD devices (50 nm compared 10 nm) it is more difficult for the gate to turn off passivation-related charge at the back surface of the TFT [44]. However, the PLD ZnO devices with Al_2O_3 gate dielectric behave differently. Considering only the high current portion of the characteristics the device shows a shift of about -15 V. This large shift is not consistent with the larger capacitance of the Al_2O_3 gate dielectric compared to SiO_2 . We do not have a simple explanation for the

large shift, however comparisons of these devices has motivated work with more similar PLD and PEALD device structures, especially identical active layer thicknesses.

The RR2 experiment involved both groups exchanging process recipes for their nominal growth structures; specifically the films were annealed at 400 °C in air for 1 hour at AFRL, according to AFRL's nominal process recipe. The samples as modified from the baseline process are shown in Figure 11. A direct comparison was made between unannealed and annealed thin and thick ZnO active layers for both growth techniques. The structures compared are listed below.

- 5) PEALD Al_2O_3 – 30 nm/ PEALD ZnO – 50nm, annealed at 400 °C
- 6) PEALD Al_2O_3 – 30 nm/ PEALD ZnO – 10nm, annealed at 400 °C
- 7) PECVD SiO_2 – 25 nm/ PLD ZnO – 50nm, annealed at 400 °C (baseline AFRL structure)

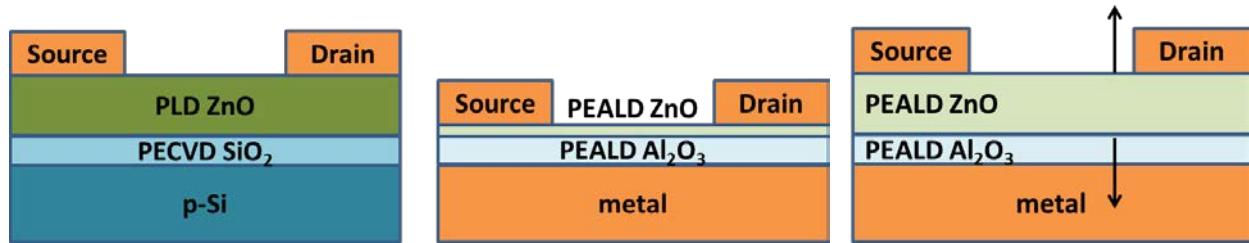


Figure 11. Second round-robin experiment where the layer thickness for the ZnO active layers were matched to the baseline structures for different PEALD and PLD processes and annealed at 400 °C.

A summary of the transfer characteristics comparison is shown in Figure 12 for pre- irradiation and post-irradiation for device structures #5, 6, and 7. Device structure #7 baseline AFRL, Figure 12(left), show the best electrical performance pre-irradiation. Device structures #5 and 6 showed almost no hysteresis pre-irradiation with the 400 °C anneal, as shown in Figure 12 (middle, right). This is different from unpassivated, un-annealed PEALD ZnO TFTs where a hysteresis is always seen before passivation. While the 400 °C anneal reduced the hysteresis, the electrical properties were not improved namely field-effect mobility was $<10 \text{ cm}^2/\text{V-s}$ in both cases. These device structures were also subjected to a 5 Mrad gamma-ray dose exposure to assess the radiation-hardness on annealed devices. PLD ZnO TFT radiation-induced shift was as expected, $\Delta V_{\text{ON}} = -2.2 \text{ V}$, corresponding to an induced charge of $\Delta Q = 1.6 \times 10^{12} \text{ cm}^{-2}$. PEALD ZnO TFTs with 50 nm active layer show a smaller V_{ON} shift, -1.3 V, when correcting for capacitance, the radiation induced charge is $\Delta Q = 1.8 \times 10^{12} \text{ cm}^{-2}$. PEALD ZnO TFTs with 10 nm active layer showed nearly no radiation-induced V_{ON} shift after 5 Mrad. However, the devices show some hysteresis post-irradiation. A complete study of layer thickness variation with radiation is shown later pointing to active layer/passivation interface as the key radiation-induced change.

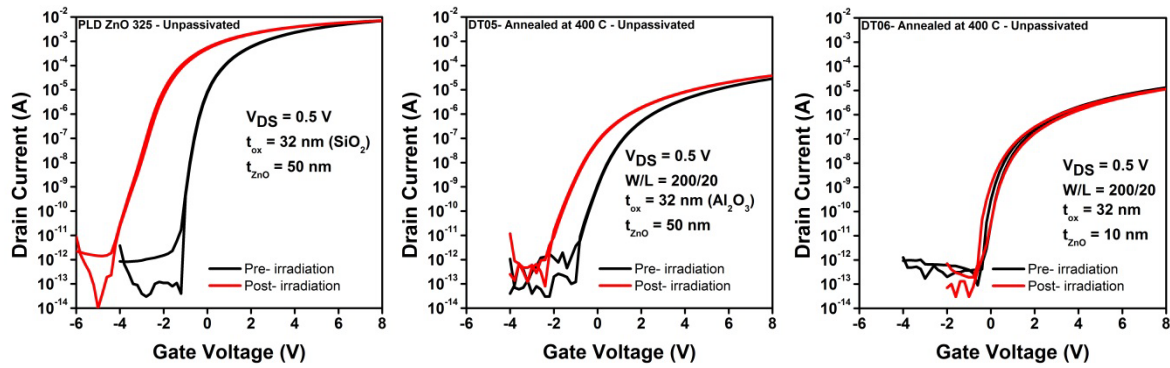


Figure 12. Transfer characteristics of unpassivated TFTs for ZnO layers grown on both PEALD Al_2O_3 and PECVD SiO_2 gate-dielectrics annealed at 400 °C for 1 hour. Black curves show device performance before irradiation and red curves show post-5 Mrad irradiation.

The initial sample and process exchange experiments produced device structures for electrical and spectroscopic characterization to understand fundamental differences in material growth, interfaces and processing conditions in materials with similar electrical performance. These experiments helped to understand differences in interfaces between gate dielectrics and ZnO layers grown by PEALD and PLD and led to a down-select of dielectric and active layer thickness combinations for use in further studies. The variations observed in passivation experiments have also led us to focus on a small subset of passivation or tri-layer passivation techniques for future irradiation experiments to better distinguish between passivation/interface phenomena and radiation effects.

The second year focused on the design of a mask set including process control monitor (PCM) structures for the analysis of 1) radiation effects in TFTs, 2) Metal/gate dielectric, gate dielectric/active layer, active layer/passivation layer interfaces, 3) Contact barrier to active layer, and 4) in-situ electrical irradiation characterization. A picture of the 2 cm x 2 cm die is shown in Figure 13.

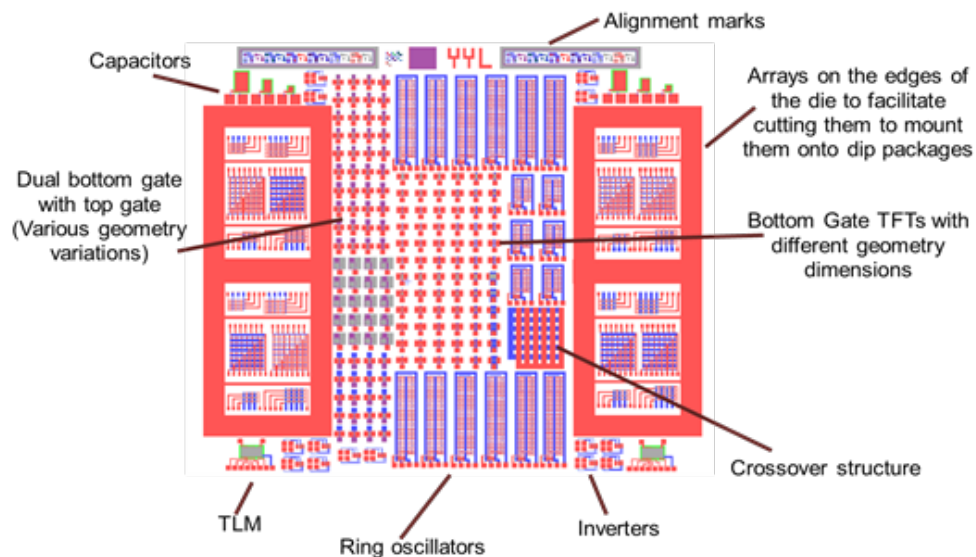


Figure 13. A picture of a die of the mask design for PSU and AFRL ZnO TFTs with various structures ranging from simple isolation structures to ring-oscillators.

The mask consists of discrete TFT structures with bottom-gated and dual-gated structures of varying width/length ratios. In addition to standard TFT structures, dual bottom-gated TFTs with an additional top-gate are included to deconvolve interface states, channel turn-on, and contact turn-on. Experimental data from this structure helped us have a more comprehensive device model. A cross-sectional view of this TFT is shown in Figure 14. Standard PCM structures such as capacitors with different geometries are included to evaluate different gate dielectrics and gated transmission-line measurement (TLM) structures are included to measure contact resistance and assess radiation effects. The mask also includes simple circuits like inverters and ring oscillators. Ring oscillators are good indicators of radiation effects due to sensitivity to device variations.

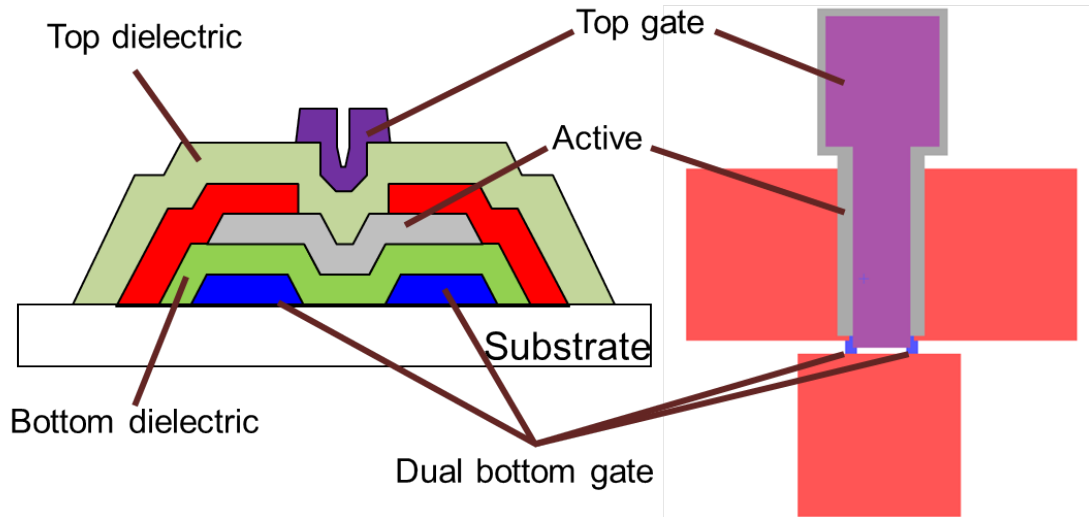


Figure 14. Discrete TFT structure with bottom dual gate to suppress contact barrier and top gate for channel turn-on.

Initial work focused on obtaining material and device baselines and irradiating these structures to down-select the number of material and device combinations for in-situ measurements. In order to have reasonable statistics on device characteristics new hardware integration and software was developed to measure groups of devices under one cumulative irradiation dose. Figure 15 shows the various array sizes including 3x3, 4x4, and 7x7. The arrays are mountable in 16-pin dip packages.

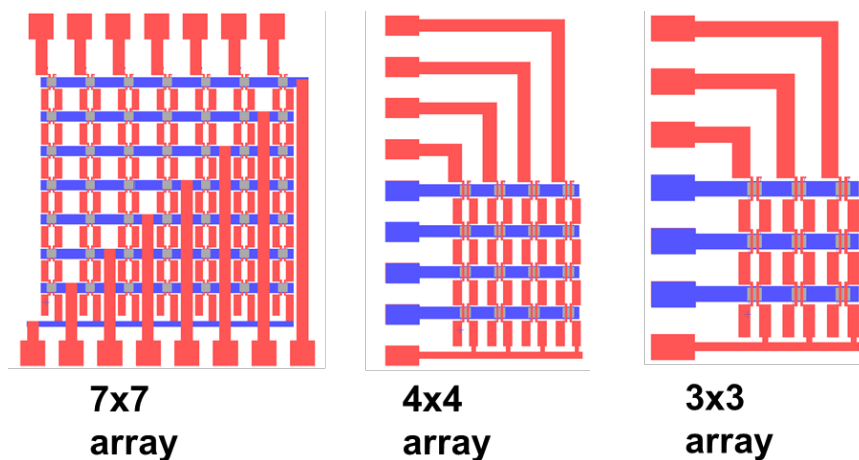


Figure 15. Different array sizes with varying W/L ratios to fit in a 16-pin dip package for in-situ measurement under irradiation.

The key outcome this activity was improved ability to measure devices in-situ during irradiation. The previous mask design was limited to measuring up to three devices at a time. Current capability allows up to 16 devices to be measured per irradiation experiment. This new capability combined with the standard PCM structures provides a more complete data set for physical device modeling.

Electrical Characterization of Irradiated Devices and Development of In-Situ measurement Techniques

Gamma and Neutron Radiation Testing on ZnO TFTs with Hf₂O Gate Dielectric

In the previous section we showed various material permutations used in TFT stacks. While some of these devices show undesired electrical characteristics (hysteresis and high subthreshold slope), exposing these devices to gamma and neutron radiation was useful to understand material stack qualities affect radiation-induced effects and the importance of selecting a robust material stack for subsequent TFT radiation experiments.

Unpassivated PLD ZnO TFTs with HfO₂ gate dielectric were exposed to 10 Mrad ⁶⁰Co. Log(I_b) versus V_{GS} at V_{DS} = 0.5 V characteristics are shown in Figure 16 for pre- and post- irradiation. The device layers are a 44 nm ZnO active layer on top of a 30 nm HfO₂ gate dielectric. Devices with total periphery of 400 μm and gate length of 5 μm were measured before and after exposure. Even prior to irradiation, the devices with HfO₂ gate dielectric were less stable, exhibiting hysteresis in the transfer curves. After a 10 Mrad gamma exposure, the hysteresis increased by several volts. However, threshold current was not affected significantly as indicated by a small change in V_T. Mobility did not degrade with irradiation. A short bake at 200 °C for 1 minute in air did not reverse the changes induced by irradiation, though the hysteresis observed did decrease. This gate dielectric is currently one of the least stable as deposited. It is unclear whether defects and traps are in the dielectric or at the dielectric/semiconductor interface. Therefore, this gate dielectric was discontinued to avoid confusion between material-related issues and radiation effects.

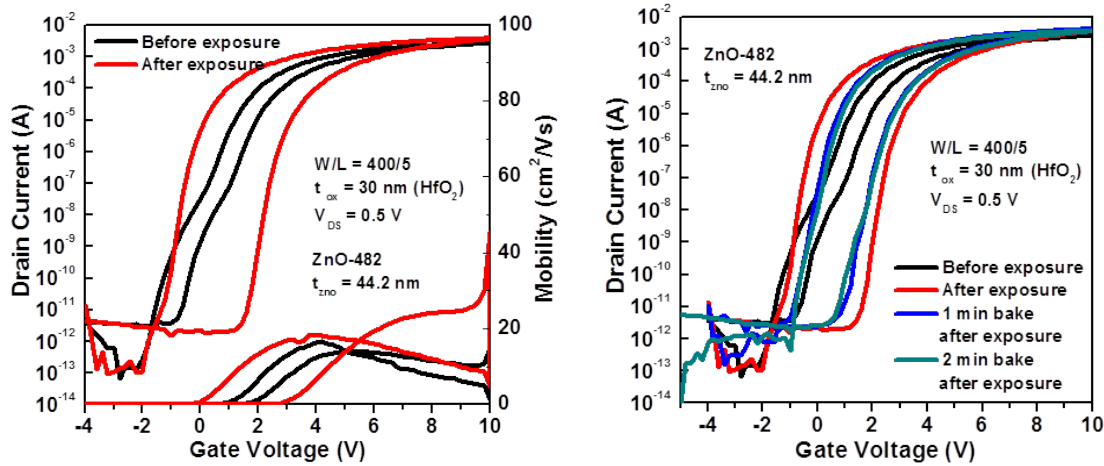


Figure 16. 10 Mrad gamma exposure of PLD ZnO TFTs with HfO₂ gate dielectric. Before and after irradiation transfer characteristics are shown on the left. Transfer characteristic changes after short anneal at 200 °C are shown on the right. Hysteresis in the data complicates analysis of radiation effects.

ZnO devices with Hf_2O_3 gate dielectric were also exposed to fast neutrons for preliminary information. In this set of experiments samples were exposed to two different times equivalent to 3.3 Mrad (SiO_2) and 10 Mrad (SiO_2). Irradiation results on unpassivated PLD ZnO TFTs with HfO_2 gate dielectrics are shown in Figure 17. The device layers are a 44 nm ZnO active layer on top of a 30 nm HfO_2 . Devices with total periphery of 400 μm and gate length of 5 μm were measured before and after exposure. As in the gamma radiation case, the TFTs with HfO_2 gate dielectrics were unstable before and after neutron irradiation. Device hysteresis was unstable and no meaningful conclusion could be drawn about the impacts of neutron irradiation. This device structure was not used in any further radiation experiments.

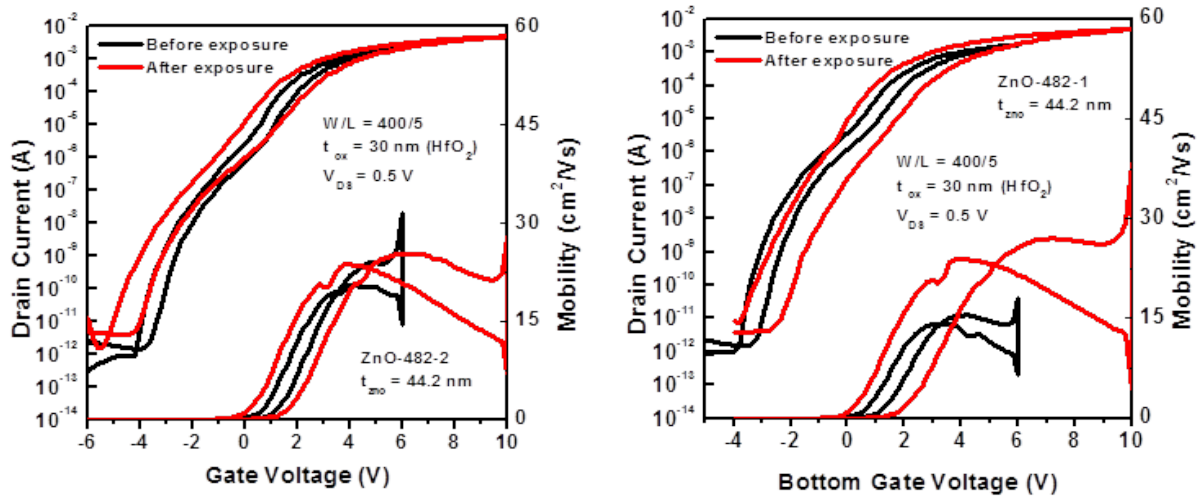


Figure 17. Unpassivated PLD ZnO TFTs with HfO_2 gate dielectrics exposed to 3.3 Mrad (LEFT SIDE) and 10 Mrad (RIGHT SIDE) fast neutrons. Extreme instability and hysteresis prevent meaningful interpretation.

Gamma and Neutron Radiation on ZnO TFTs with Al_2O_3 and SiO_2 Gate Dielectric

Current-voltage characteristics for PEALD and PLD TFTs were measured before and after 10 Mrad ^{60}Co gamma ray exposure. For both device types the TFTs function after gamma ray exposure with little change in mobility or off-current. Figure 18 shows $\log(I_{\text{DS}})$ versus V_{GS} characteristics at $V_{\text{DS}} = 0.5\text{V}$ for a PEALD ZnO TFT with dimensions $W / L = 200 \mu\text{m} / 20 \mu\text{m}$ for a device before irradiation, after 10 Mrad ^{60}Co gamma ray irradiation, and after irradiation followed by a 200 $^\circ\text{C}$ anneal in air for 1 minute. The turn-on voltage, V_{ON} , for devices before irradiation is -2 V and the threshold voltage, V_{T} , is -0.6 V. After irradiation there is a -0.9 V shift in V_{ON} and a smaller, -0.6 V, shift in V_{T} . The extracted linear region field-effect mobility is $\sim 15 \text{ cm}^2/\text{V}\cdot\text{s}$ before and after irradiation.

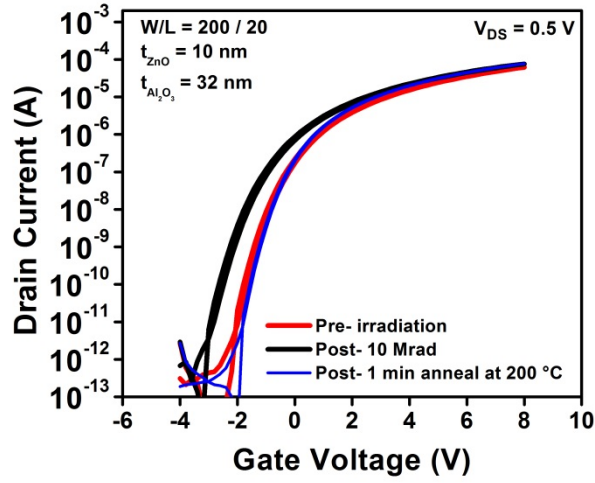


Figure 18. Linear region $\log(I_D)$ versus V_{GS} for a PEALD ZnO TFT before irradiation, after 10 Mrad ^{60}Co gamma ray irradiation, and after irradiation and a 200 °C, 1 min anneal in air.

Figure 19 shows $\log(I_{DS})$ versus V_{GS} characteristics at $V_{DS} = 0.5\text{V}$ for PLD ZnO TFTs with dimensions $W / L = 400 \mu\text{m} / 10 \mu\text{m}$ for a device before irradiation, after 10 Mrad ^{60}Co gamma ray irradiation, and after irradiation followed by a 200 °C anneal in air for 1 minute. The turn-on voltage, V_{ON} , for devices before irradiation is -0.9 V and the threshold voltage, V_T , is 0.2 V. Linear region field-effect mobility before irradiation is $60 \text{ cm}^2/\text{V-s}$. Device characteristic changes after 10 Mrad ^{60}Co gamma ray irradiation for PLD ZnO TFTs are similar to PEALD ZnO TFTs. The linear field-effect mobility, accounting for an irradiation induced negative V_T shift, decreased slightly to $55 \text{ cm}^2/\text{V-s}$ (<10% decrease). After irradiation the PLD ZnO TFTs had a V_{ON} shift of -3.4 V and a V_T of -1.8 V.

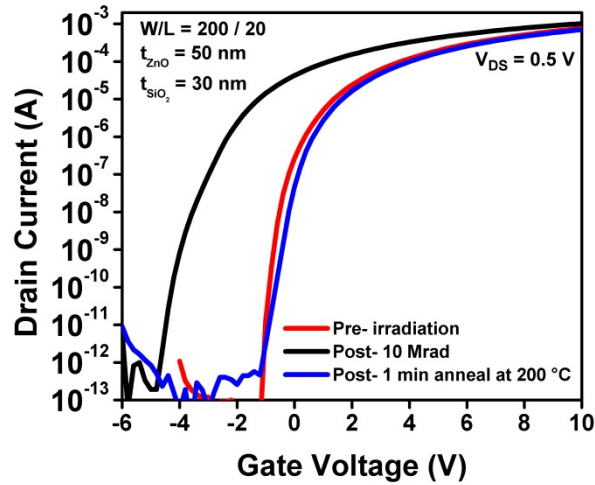


Figure 19. Linear region $\log(I_D)$ versus V_{GS} for a PLD ZnO TFT before irradiation, after 10 Mrad ^{60}Co gamma ray irradiation, and after irradiation and a 200 °C, 1 min anneal in air.

The larger irradiation-induced shift in V_{ON} than V_T can be explained by assuming that irradiation results in charge at the back of the ZnO active layer (that is, the ZnO interface farthest from the gate). In earlier work related to passivation of ZnO TFTs we found by two-dimensional modeling that a charge sheet at the back interface results in a larger shift in V_{ON} than V_T . A back interface charge model can also explain the larger shift in V_{ON} for PLD ZnO TFTs with irradiation than for PEALD ZnO TFTs. Charge at the back interface acts across the series combination of gate dielectric and depleted ZnO layer capacitances. For the PEALD TFTs with 32 nm thick Al_2O_3 gate dielectric and 10 nm thick ZnO active layer and using $\epsilon = 8\epsilon_0$ for Al_2O_3 and ZnO gives a capacitance of 180 pF/cm². For the irradiation induced V_{ON} shift of 0.9 V this a charge of $\Delta Q = C \cdot \Delta V_{ON}$ of 1×10^{12} electronic charges/cm². For the PLD TFTs with 30 nm thick SiO_2 gate dielectric and 50 nm thick ZnO active layer and using $\epsilon = 3.9\epsilon_0$ for the SiO_2 and $\epsilon = 8\epsilon_0$ for the ZnO gives a capacitance of 61 pF/cm². For the irradiation induced V_{ON} shift of -3.4 V this a charge of $\Delta Q = C \cdot \Delta V_{ON} = 1.3 \times 10^{12}$ electronic charges/cm². This suggests the apparent larger shift in V_{ON} for PLD ZnO TFTs is related to the smaller capacitance per unit area in this structure, but when converted into charge per unit area, the radiation-induced shifts are fairly similar for both device types. Table 1 summarizes the comparison between PEALD and PLD ZnO TFTs exposed to 10 Mrad ⁶⁰Co gamma ray irradiation.

	ΔV_{ON} (V)	ΔV_T (V)	Field effect mobility (cm ² /V-s)		ΔQ (/cm ²) (Induced by radiation)
PEALD ZnO TFTs	-0.9	-0.6	15	15	1×10^{12}
PLD ZnO TFTs	-3.4	-1.8	55	60	1.3×10^{12}

Table 1. Comparison of device characteristics for PEALD and PLD ZnO TFTs before and after 10 Mrad exposure.

Unbiased Neutron Radiation Testing on ZnO TFTs

Irradiation results on unpassivated PLD ZnO TFTs are shown in Figure 20. The device layers are a 48 nm ZnO active layer on top of a 30 nm SiO_2 gate dielectric. Devices with total periphery of 400 μ m and gate length of 10 μ m were measured before and after exposures of 3.3 and 10 Mrad (SiO_2). Transfer characteristics were measured at $V_{DS} = 0.5$ V while sweeping V_{GS} from -4 – +10 V. After the 3.3 Mrad exposure, the devices exhibit a V_T shift of -1.2 V while the peak mobility values remain unchanged. After the 10 Mrad exposure, V_T remains the same and the peak mobility values are again unchanged. However, there is an increase in hysteresis post- irradiation.

The same phenomenon is observed during neutron irradiation of passivated PEALD ZnO TFTs as shown in Figure 21. In this case, the device periphery was 200 μ m with gate length of 20 μ m. The device layers are a 10 nm ZnO active layer on top of a 32 nm Al_2O_3 gate dielectric, passivated with 30 nm of Al_2O_3 . The change in V_T after the 3.3 Mrad exposure is -1.5 V. The change in V_T after the 10 Mrad exposure is -0.3 V. In both cases, the smaller change in V_T with increasing dose may be caused by self-healing of the ZnO layer as the temperature increases during fast neutron irradiation.

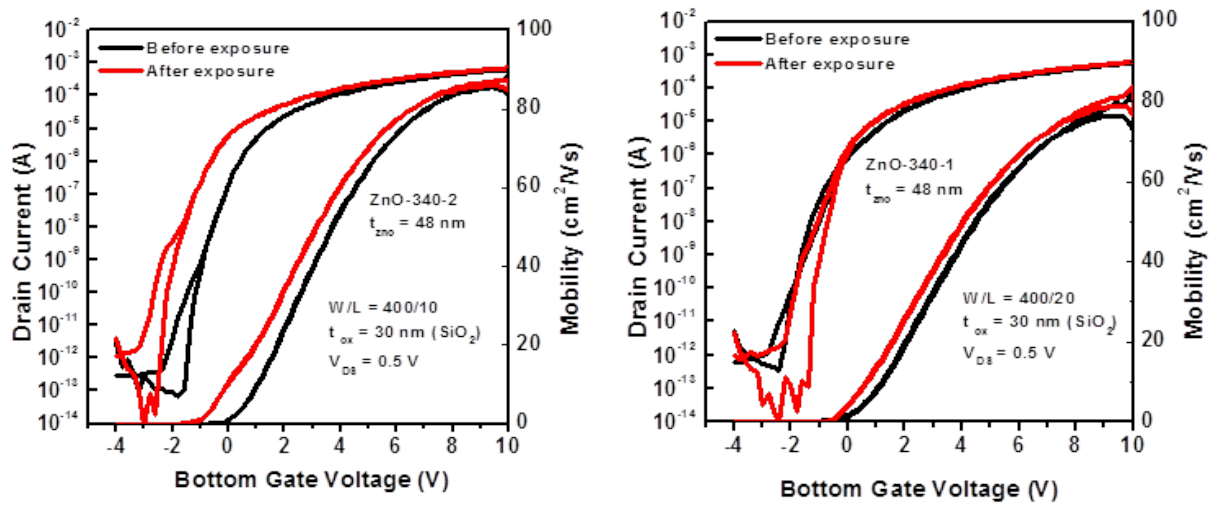


Figure 20. Unpassivated PLD ZnO TFTs exposed to 3.3 Mrad (LEFT SIDE) and 10 Mrad (RIGHT SIDE) fast neutrons. After higher doses of radiation, the change in V_T decreases substantially (in this case, goes to zero) while peak mobility values are unchanged throughout. The higher doses exhibit signs of self-healing due to increased temperature over longer exposures.

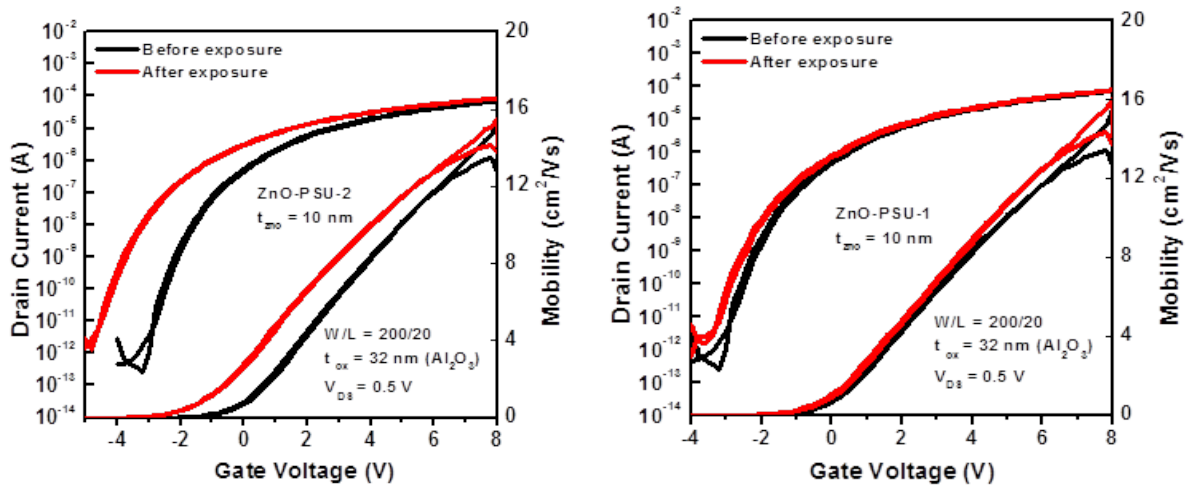


Figure 21. Passivated PEALD ZnO TFTs exposed to 3.3 Mrad (LEFT SIDE) and 10 Mrad (RIGHT SIDE) fast neutrons. After higher doses of radiation, the change in V_T decreases substantially while peak mobility values are unchanged throughout. The higher doses exhibit signs of self-healing due to increased temperature over longer exposures.

In-situ test development

Hardware and Software Setup

In response to the need to perform in-situ biased electrical characterization of devices during irradiation, the objective of this activity was to build multiplexing capabilities for in-situ TFT measurements. In-situ bias testing is required to analyze the impact of bias on the particular radiation defect formation mechanisms. For silicon MOSFETs electrical bias during irradiation can significantly

modify radiation effects. Because the charge collection volume for oxide thin film transistors is very small, we expect the effect of electrical bias during irradiation to be less. For oxide TFTs, both electrical stress and radiation exposure can cause changes in TFT characteristics, so it is important to measure the effects of each.

Over the course of the program we developed two different capabilities for in-situ temperature monitoring and DC-IV device characterization during irradiation for the ^{60}Co source and neutron reactor. The first iteration of measurement capabilities used an HP 4141B and Keithley 708A switch matrix controlled by LabView. Figure 22 shows the sample fixture with integrated thermocouple used for in-situ radiation experiments and sample fixture loaded into ^{60}Co gamma cell. The drawback of this first generation measurement setup was that only up to 3 devices could be measured during an experiment. While the first-generation of measurement capabilities provided us with initial results, we developed a second generation of measurement capabilities expanding the number of DUTs.

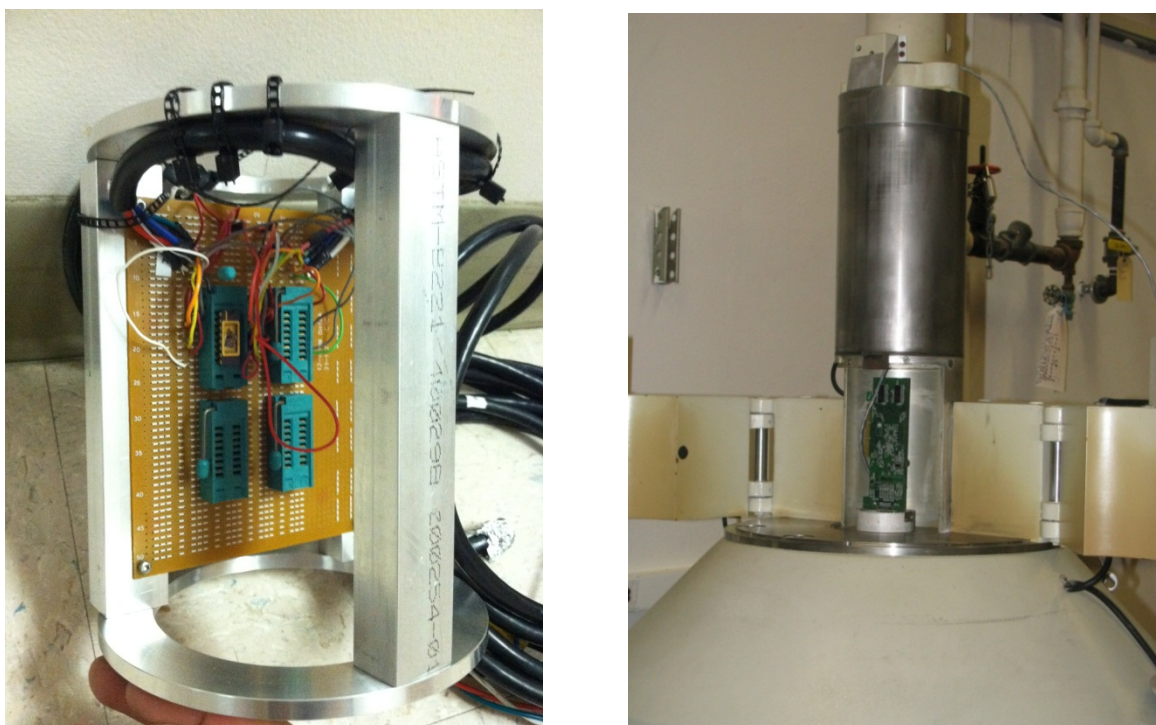


Figure 22. Left side: In-situ bias sample fixture with integrated thermocouple. Right side: Sample fixture loaded in ^{60}Co gamma cell.

The new test setup is capable of supporting the 4x4 arrays included on the new mask set. The previous test equipment used a HP4141B DC source/monitor and a Keithley 708A switching system, limiting characterization to only three devices per exposure. The second generation of measurement equipment was upgraded to a Keithley 7075 multiplexer card, as shown in Figure 23. Adding the Keithley 7075 multiplexer card with eight 1x12 banks resulted in the ability to measure up to 16 devices during irradiation.

Custom software was developed in Visual C++ to support measurement of $I_{DS} - V_{GS}$ sweeps and I_{DS} - time. New capabilities were added to increase device-under-measurement count and measure full arrays of devices. Groups of devices can be biased in saturation while other groups of devices can be biased in the linear region all during the same exposure. Additionally, the sampling period has been reduced from ~ 1800 seconds to ~ 140 seconds when compared with the original equipment and software. The timing diagrams for both the old and new configuration are shown in. For the arrayed TFTs, I_{DS} versus V_{GS} is measured by sweeping a row with one column held at a given V_{DS} . During this sweep, the other rows are held at $V_{GS} = -6$ V (OFF state) and the other columns at $I_{DS} = 0$. Different drain biasing conditions can be selected for the different drain lines. The gate leakage current is also monitored on every device. The software can be modified in almost real-time to customize bias conditions. The current software version is configured to measure a 4x4 array.

The outcome was the ability to generate statistically significant measurements of bias effects in irradiated devices. This is a requirement to identify physical mechanisms responsible for changes in electrical performance and self-healing. The new system offers increased measurement flexibility in terms of bias conditions and number of samples.



Figure 23. Test setup for in-situ measurement of ZnO TFTs modified for increased multiplexing capabilities.

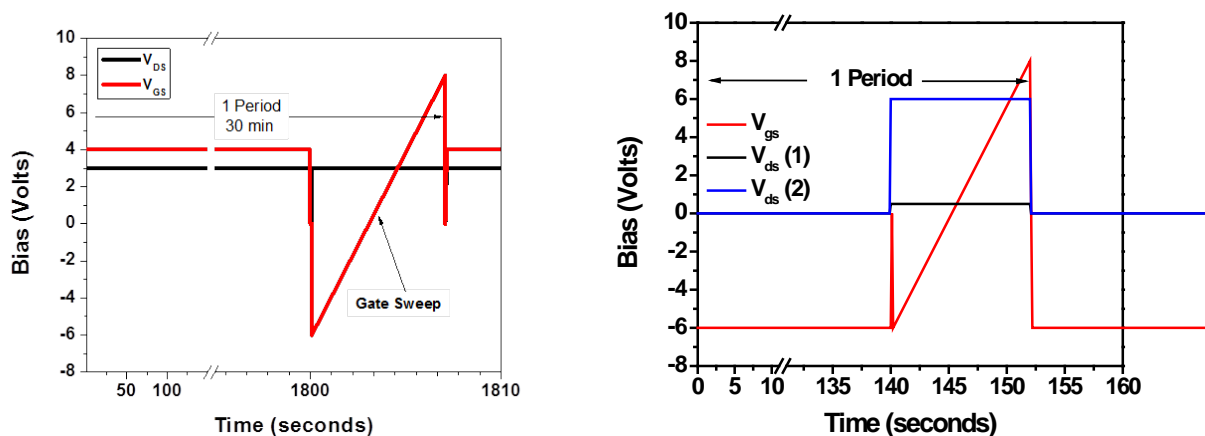


Figure 24. The original timing diagram shown on the left is from the prior period of performance and limited to a sampling rate of about 30 minutes. The timing diagram on the right depicts the system improvements with sampling rates of about 2 minutes and multiple drain bias configurations.

In-situ Bias Testing of ZnO TFTs while Irradiated

The objectives of this task were to demonstrate large-scale data collection of devices that are biased in-situ during irradiation and compare changes in transfer characteristics and gate leakage before, during, and after irradiation. In this experiment, a 4x4 PEALD ZnO TFT array as shown in Figure 25 was irradiated with ^{60}Co at the Breazele Reactor at Penn State University. ZnO TFTs with $W/L = 100/5\text{ }\mu\text{m}$ were irradiated up to 25 Mrad with an approximate dose rate of $\sim 600\text{ krad/hr}$. The TFTs were biased at two different drain-bias voltage, in the subthreshold region $V_{\text{DS}} = 0.5\text{ V}$ and in the saturation region $V_{\text{DS}} = 6\text{ V}$. Each device was measured every $\sim 140\text{ secs}$. The timing diagram for the data collection is shown on the right side of Figure 24. Data was collected for non-irradiated, baseline samples with electrical stress only and compared to evolutionary data for devices under irradiation. The pre- and post-irradiation electrical characteristics are compared. Characterizing and controlling measurement artifacts are critical.



Figure 25. Optical microscope image of 4x4 TFT array used for testing shown on the left with zoom-in of active device area shown on the right.

A control experiment is required to differentiate electrical stress effects on ZnO TFTs in the presence and absence of radiation. Results from the control experiment to collect baseline data for TFTs under electrical stress are shown in Figure 26. Transfer characteristics are shown for two different drain biases ($V_{\text{DS}} = 0.5\text{ V}$ and 6.0 V) during a DC stress test over 50 hours. The OFF-current noise at negative gate bias measured in these devices is an artifact of the cables used in this measurement. Normal OFF-current levels for devices measured on-wafer is orders of magnitude lower. The devices showed no significant degradation in subthreshold slope or on-current. The most significant change seen for both drain bias conditions was a *positive* V_{ON} shift of $\sim +0.5\text{ V}$ as a function of time. This *positive* shift will become important when observing the devices during irradiation.

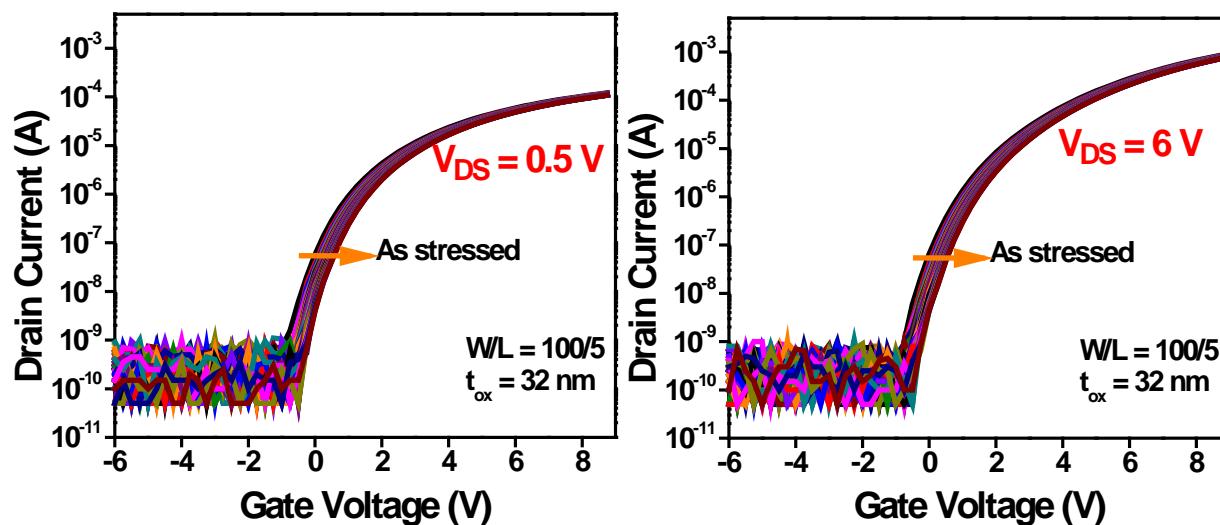


Figure 26. Transfer characteristics of ZnO TFTs during electrical stress only for 50 hours. Devices biased at (left) $V_{DS} = 0.5 \text{ V}$ and (right) $V_{DS} = 6 \text{ V}$.

In-situ DC stress tests for devices biased at $V_{DS} = 0.5 \text{ V}$ and $V_{DS} = 6.0 \text{ V}$ and were conducted for devices under irradiation up to a cumulative dose of 25 Mrad. Figure 27 shows transfer characteristics for devices before, during, and after irradiation. The transfer characteristics pre-irradiation are similar to those obtained for non-irradiated samples. However, there are significant differences during irradiation. There is a large change in subthreshold current. This subthreshold current increases as a function of time, but completely recovers as soon as the TFTs are taken out of the cell. The source of this current appears to be gate leakage as seen in Figure 28. However, the gate leakage current increases by the same order of magnitude that the subthreshold current increases and completely recovers as soon as the radiation is stopped. During the course of the experiment, V_{ON} has a several volt *negative* shift. After radiation is stopped, V_{ON} remains shifted by -1.0 V. The final *negative* V_{ON} shift is a true effect of the radiation. We believe the in-situ V_{ON} shift of several volts and increase in subthreshold current to be an artifact of cable charging or other in-situ ionization effects in the reactor that do not permanently change the device characteristics, as shown next.

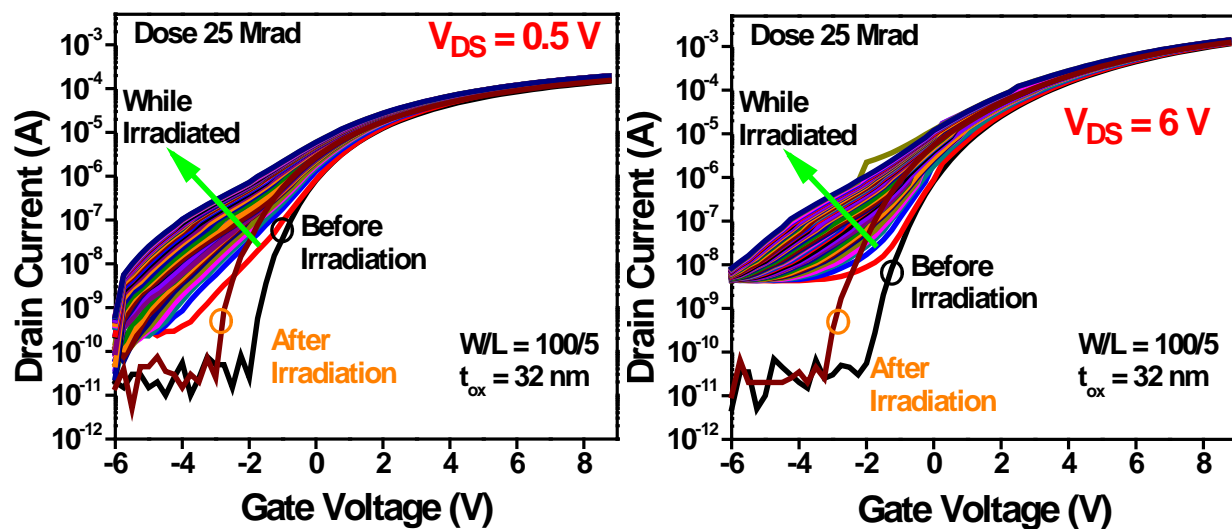


Figure 27. Transfer characteristics of ZnO TFTs before, during, and after irradiation for devices biased at (left) $V_{DS} = 0.5$ V and (right) $V_{DS} = 6$ V. The cumulative dose was 25 Mrad.

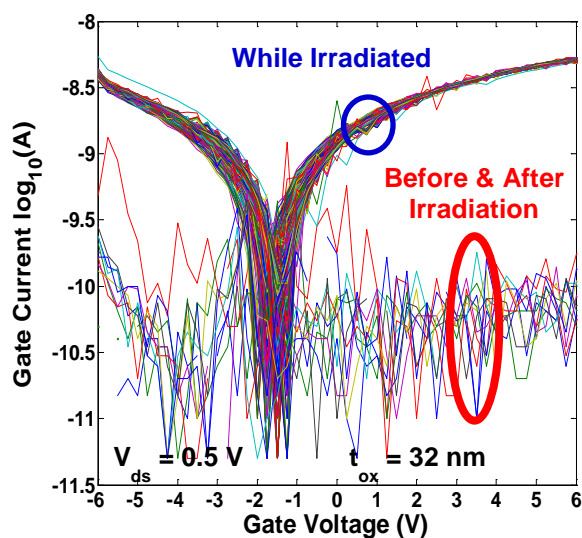


Figure 28. Gate leakage current before, during, and after 25 Mrad irradiation of ZnO TFTs

Figure 29 compares before and after electrical bias transfer characteristics of TFTs stressed for 50 hours. A direct comparison is made between devices biased at $V_{DS} = 6.0$ V and $V_{DS} = 0.5$ V. A small positive change in V_{ON} (~ 0.5 V) is seen for both bias conditions. The subthreshold slope and saturation current do not change. This is indicative that V_{ON} shift might be related to negative charge trapping in the gate dielectric as a function of time (stress time).

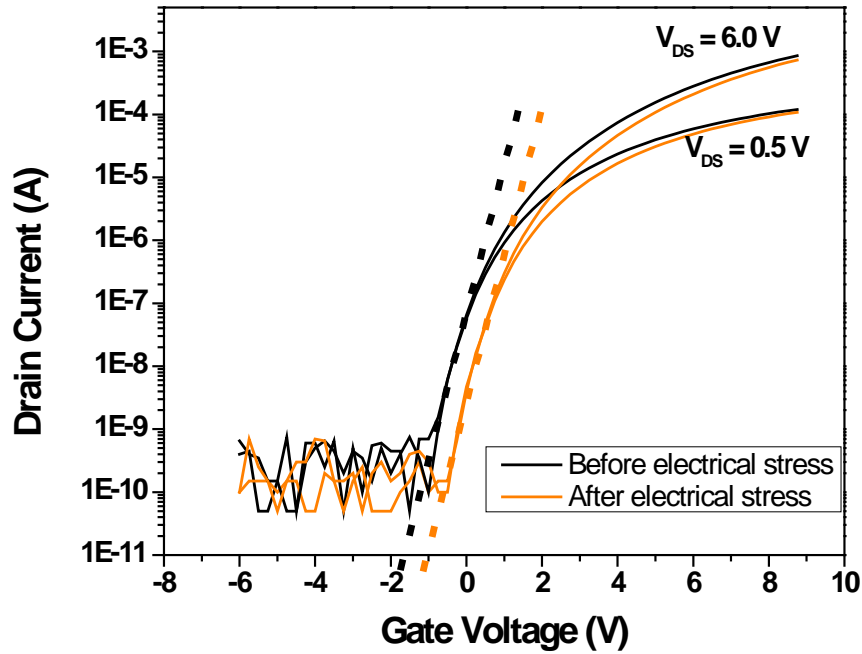


Figure 29. Before and after electrical bias transfer characteristics of TFTs stressed for 50 hours. A direct comparison is made between devices biased at $V_{DS} = 6.0$ V and $V_{DS} = 0.5$ V. A small positive change in V_{ON} is seen for both bias conditions. The subthreshold slope and saturation current do not change.

Figure 30 shows pre- and post-irradiation transfer characteristics of TFTs with 25 Mrad cumulative dose. A direct comparison is made between devices biased at $V_{DS} = 6.0$ V and $V_{DS} = 0.5$ V. The change in V_{ON} is identical for both bias conditions. The saturation current converges to the same value pre- and post-irradiation values suggesting nearly no change in V_T post-irradiation but only a change in V_{ON} . The subthreshold slope is the same pre- and post-irradiation for both bias conditions.

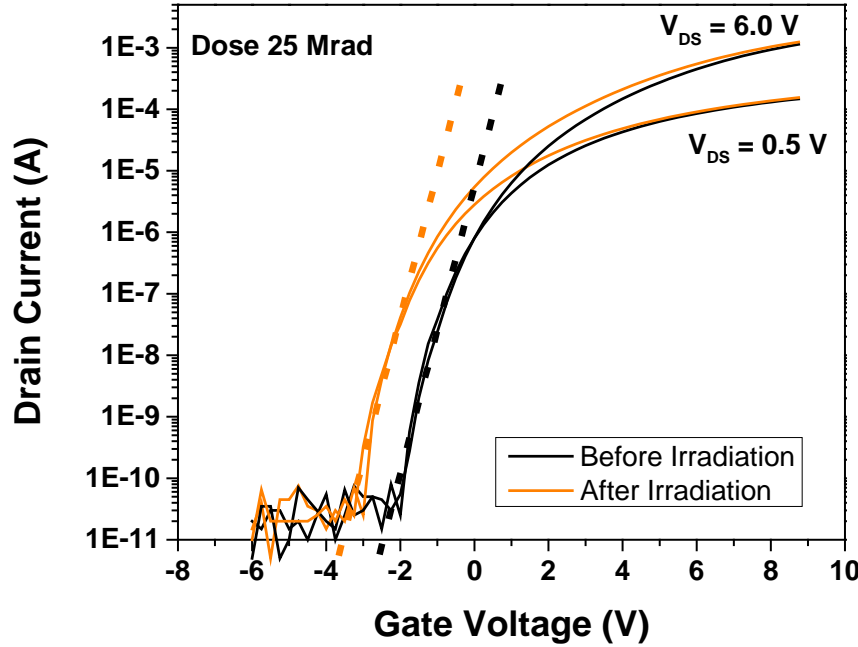


Figure 30. Pre- and post-irradiation transfer characteristics of TFTs with 25 Mrad cumulative dose. A direct comparison is made between devices biased at $V_{DS} = 6.0$ V and $V_{DS} = 0.5$ V. The change in V_{ON} is identical for both bias conditions. The saturation current converges to the same value pre- and post-irradiation values. The subthreshold slope is also the same pre- and post-irradiation for both bias conditions.

A comparison of field-effect mobility ratio extracted from devices under electrical stress only and electrical stress with 25 Mrad dose is shown in Figure 31. Field-effect mobility is nearly unchanged for devices under electrical stress only, which indicates V_T is unchanged during electrical stress. For TFTs under electrical stress and irradiation an apparent increase in field-effect mobility is seen while irradiated. However, we believe this is an artifact of an apparent change in V_T convoluted with the increase in subthreshold current because the field-effect mobility returns to its initial, pre-irradiation value, post-irradiation.

Contributing factors for this phenomenon include 1) the ionization of the surroundings (air) contributing to positive charge on the surface of the TFT and 2) the off-state negative gate bias applied to devices between sweeps attracting ionized charge to the interface. Further experiments were carried out to differentiate these effects including adding a ground plate to the top of the device to add another degree of control over the channel charge.

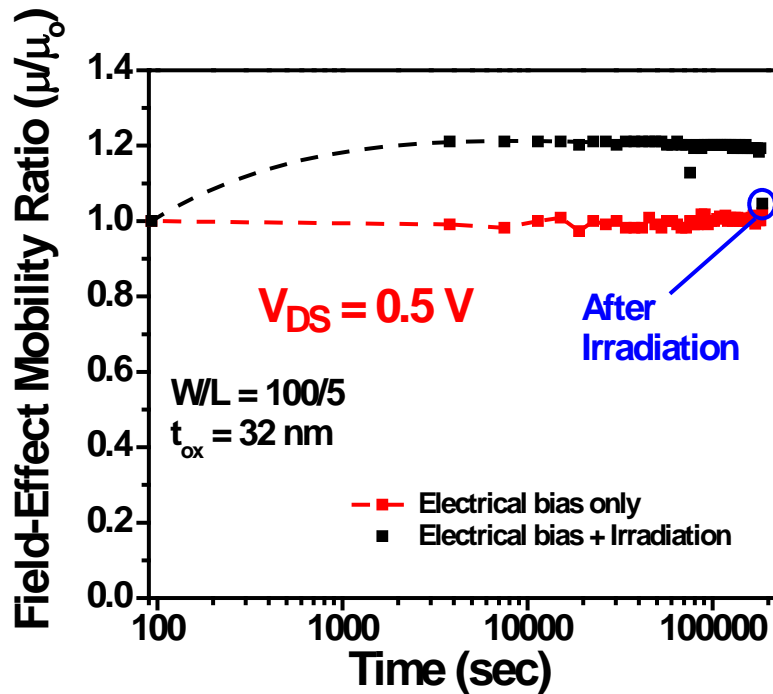


Figure 31. Comparison of field-effect mobility for electrical stress only and electrical stress with 25 Mrad cumulative dose. No change in mobility for devices with electrical bias only. An apparent increase in mobility, for devices with electrical bias and 25 Mrad cumulative dose, while irradiated is believed to be an artifact and post-irradiation mobility is the same as measured pre-irradiation.

The key outcomes for this activity are the measurement of statistically significant devices in-situ during irradiation and the observation that ZnO TFTs show very limited degradation under bias during irradiation unlike other TFTs. These experiments have also revealed the need to do further experiments to characterize potential systemic issues such as cable charging and ionization in the reactors and differentiate these effects from radiation effects.

Measurement Artifacts

During irradiation the TFT low-current characteristics, including the apparent off-current and the subthreshold characteristics near V_T , are significantly perturbed. We believe this is largely due to charge collection on the surface of the TFTs and unshielded wiring in the ionizing radiation environment. During irradiation ions and electrons are created by interactions between gamma rays and the air in the irradiator. Charge is collected by the device test wiring and leads to artifacts in the low current TFT characteristics. Measurements of device test wiring with bias, but with no TFT connected, show significant leakage current inside the ^{60}Co irradiator, though not as large as the measured TFT low current effects during irradiation. We believe an additional contribution comes via charge collection at the back interface of the TFT during irradiation.

Unlike silicon MOSFETs, in bottom gate TFTs the gate electric field is not contained during all regions of device operation. For ZnO TFTs, when the device is biased to form an electron accumulation channel (the TFT on state) the gate electric field terminates on channel charge. However, when the TFT is biased in the off state the gate charge may not be balanced by minority charge (holes). For this case the gate electric field extends through the device back interface and terminates on the device contacts or other nearby features. This fringing field can also attract mobile charge, present as ions and electrons in the irradiation environment. For the TFT biased with $V_{GS} < 0$ we expect the TFT back interface to attract positive ions. This positive charge layer, which will depend on details including the irradiation ambient and time, will act to shift the apparent turn-on voltage for the TFT. The charge at the TFT back interface is not stable and may be lost when the TFT gate is biased positive or compensated by additional adventitious charge in the irradiant ambient. The charge is only partially bound and even a positive gate voltage is sufficient to remove much of the charge.

To confirm that charge at the TFT back interface plays a role in the low-current measurements during irradiation we prepared test devices with shielding added to avoid back interface charge accumulation. For this test we used PEALD ZnO TFTs with the previously described device structure. To these devices we added a $\sim 3 \mu\text{m}$ thick layer of chemical vapor deposited poly(p-xylylene) (parylene) and used silver paint, connected to ground, to provide simple shielding over the device area, as shown in Figure 32 inset. Test devices were then exposed to ^{60}Co (0.01 Mrad/hr) for 24 hours for a cumulative dose of ~ 240 krad. $\log(I_{DS})$ versus V_{GS} was measured, as shown in Figure 32. When the sample is first introduced to the irradiator there is an increase in the apparent TFT off-state current, though much less than for unshielded devices. After a few minutes of irradiation the TFT off-state current is reduced further and remains constant for the remaining cumulative dose. The initial larger off-state current may be related to charge accumulation on the measurement cables. The steady-state off-state current in the irradiator is similar to the current measured for biased device test wiring with no TFT and is likely due to charge collection in the ionizing irradiator environment.

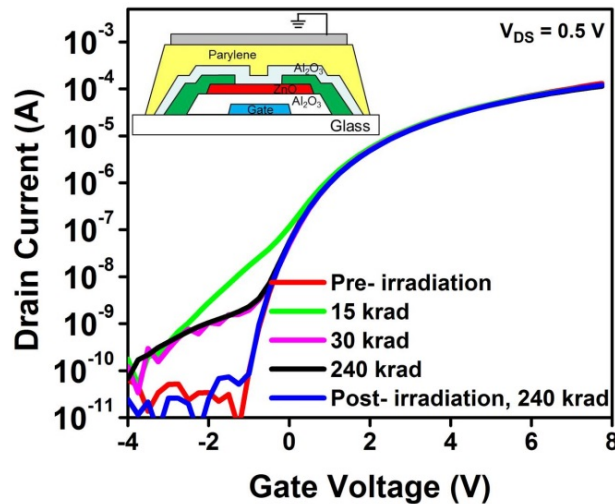


Figure 32. Insert: Bottom gate PEALD ZnO TFT (same structure as used in previous experiments) with an additional low-k dielectric and a conductive film over it connected to ground. Linear region $\log(I_D)$ versus V_{GS} for a PEALD ZnO TFT with the top surface shielded exposed to 240 krad. Anomalies in the low current region are avoided with proper shielding.

With the effects of artifacts related to the ionizing irradiation environment removed, the effect of electrical bias on gamma-ray radiation-induced changes in ZnO TFTs is very small. As shown in Figure 30, PEALD ZnO TFTs biased as described and exposed to a cumulative dose of 25 Mrad, have a V_{ON} shift of -1.1 V and V_T shift of -0.6 V. The small difference in shifts between biased and unbiased devices with irradiation is likely caused by the effects of electrical stress noted above. 25 Mrad dose required about 50 hours exposure in the irradiator used for this experiment. The control experiment of electrical stress with no irradiation resulted in V_{ON} and V_T shifts of 0.5 and 0.2 V, respectively, for 50 hours of the bias conditions used during irradiation. Subtracting the control electrical bias shift from the observed electrically biased during irradiation shifts gives V_{ON} and V_T shifts of -1.6 and -0.8 V, respectively, close to the irradiation-induced shifts observed for unbiased devices. In-situ biasing does not seem to have significant impact on device changes during irradiation and suggests the need to spend more time isolating physical mechanism and location of irradiation induced changes as opposed to bias conditions.

Results for Wide Irradiation Dose Range

Figure 33 shows the shift in TFT threshold voltage, V_T , for ^{60}Co irradiation dose up to 100 Mrad. This relatively high cumulative dose of 100 Mrad is unlikely to be reached under normal space application but underlines the intrinsic radiation hardness of ZnO TFTs. Figure 33 includes data for both biased and unbiased devices and is uncorrected for the shifts related to electrical stress. Notably, the threshold voltage shift is not linear with dose rate, but slows with increasing dose. As noted above, a short anneal at 200 °C removes most of the irradiation induced device changes and some reduction take place even at room temperature. V_T -shift recovery post- 200 °C, 1 minute anneal is shown for devices exposed to 50 Mrad. We expect that self-annealing during irradiation also affects the results. The two irradiators operate at different nominal temperatures (~34 °C for the high dose rate irradiator and ~30 °C for the low dose rate irradiator).

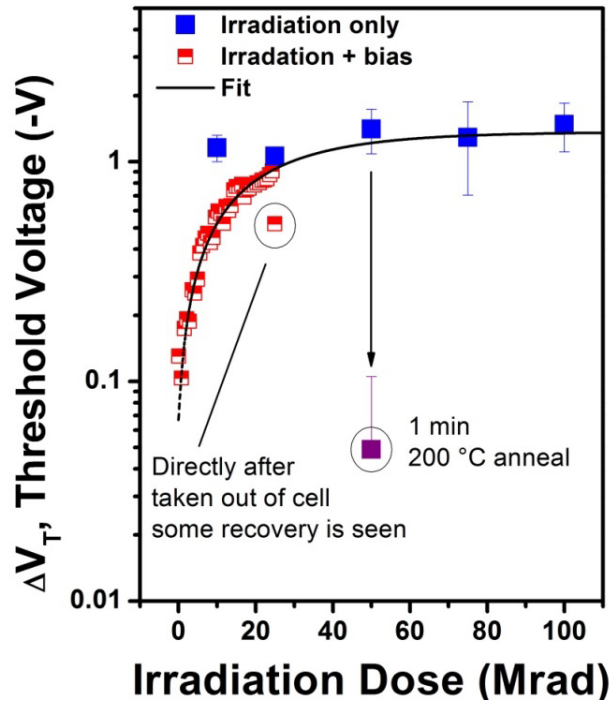


Figure 33. Threshold voltage as function of irradiation dose for irradiation only and irradiation with electrical bias for doses up to 100 Mrad. In both cases, threshold voltage is similar in both cases. 1 minute anneal at 200 °C nearly removes the radiation-induced V_T shift.

Physical Location of Radiation-Induced Changes in ZnO TFTs

While we have shown that properly designed ZnO TFTs can withstand up to 100 Mrad doses, devices show a small radiation-induced negative V_T shift indicating charge accumulation within one of the materials or interfaces. The objective of this task was to have a preliminary understanding of the physical location of the radiation-induced charge accumulated in the TFT structure. We studied the impact of surface charge and passivation, varied active layer and gate dielectric thickness and used this information to develop a model based on the experimental results. All devices were exposed to 5 Mrad gamma-ray and were evaluated in terms of induced charge on the stack ($\Delta Q = C \cdot \Delta V$). As illustrated in Figure 34, these experiments were designed to isolate changes in the top ZnO interface (left), ZnO layer itself (middle), and within the gate dielectric (right). By changing the volume exposed to radiation, a larger change in charge should occur in regions where damage is occurring.

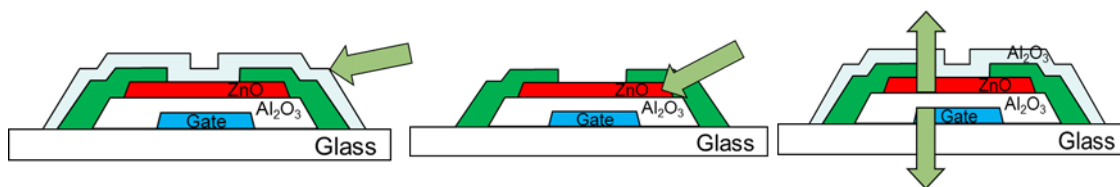


Figure 34. Multiple device permutations were studied for PEALD ZnO TFTs to understand which interface was affected the most by irradiation. Left – changes in passivation technique identify effects at the ZnO top interface; middle – changes in ZnO thickness show effects generated in the ZnO layer; right – changes in the gate dielectric thickness show effects of radiation in the gate dielectric.

This set of experiments used PEALD ZnO TFTs with a metal gate and Al_2O_3 gate dielectric because we had the most data for this material stack. Throughout the program we have emphasized the need to carefully pick a passivation layer that is robust, provides electrical stability under normal operation and radiation environments. We first studied passivation variation effects. ZnO TFTs were fabricated with a 32 nm- Al_2O_3 gate dielectric and 10 nm-ZnO active layer. Three different passivation schemes were investigated: unpassivated, ALD-passivated, and tri-layer. While a passivation layer is typically added post- device processing to improve electrical stability, devices can function without a passivation layer. The baseline device stack with ALD passivation was also included to have a comparison to our previous work. The tri-layer structure has the same material stack as the baseline device but the gate dielectric, active layer, and passivation are all grown in one step. This method prevents the channel region from being exposed to air and/or chemicals during fabrication, and giving enhanced electrical stability over post- processing ALD-passivated ZnO TFTs.

Figure 37 shows $\text{Log}(I_{DS})$ versus V_{GS} for ZnO TFTs using different passivation schemes as represented by Figure 34 (left). The V_T shift induced by 5 Mrad gamma-ray radiation is -0.14 V for unpassivated devices, -1.43 V for ALD-passivated devices, and -0.59 V for tri-layer devices. This experiment suggests that passivation variations result in significant changes in charge from radiation exposure. While unpassivated PEALD ZnO TFTs offer limited electrical stability, they appear to be the most radiation-hard. However, they are vulnerable to processing induced effects on the amount of charge collected at the ZnO/passivation interface.

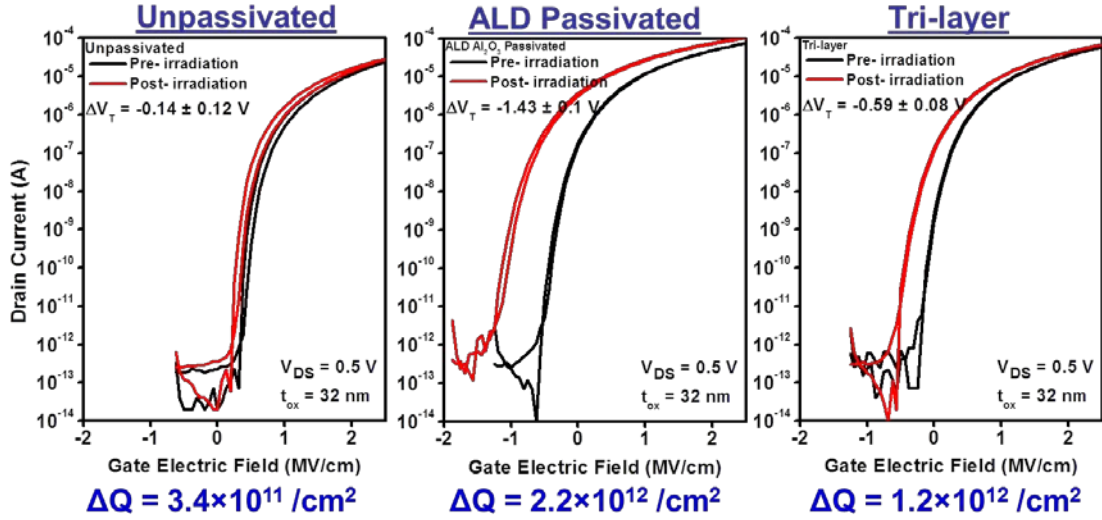


Figure 35. PEALD ZnO TFTs with different passivation schemes. Passivation variations result in significant changes in radiation-induced charge.

Next, we studied the effects of ZnO film thickness variation as in Figure 34 (middle). Three different thicknesses were chosen, 10 nm, 33 nm and 58 nm, over same thickness gate dielectric and no passivation. The reason we opted for no passivation on these PEALD-grown ZnO TFTs is because passivation of >30 nm ZnO films result in a change in the subthreshold region associated with a conductive layer at the ZnO/passivation interface. Figure 36 shows $\text{Log}(I_{DS})$ versus V_{GS} for ZnO TFTs with different active channel thicknesses. While there is a variation in charge collected by the devices between thin (10 nm) and the thicker (38-nm and 58-nm) active channels, the change in charge is significantly less than the change in charge in the passivation variation, pointing to semiconductor/passivation as the most radiation-sensitive interface.

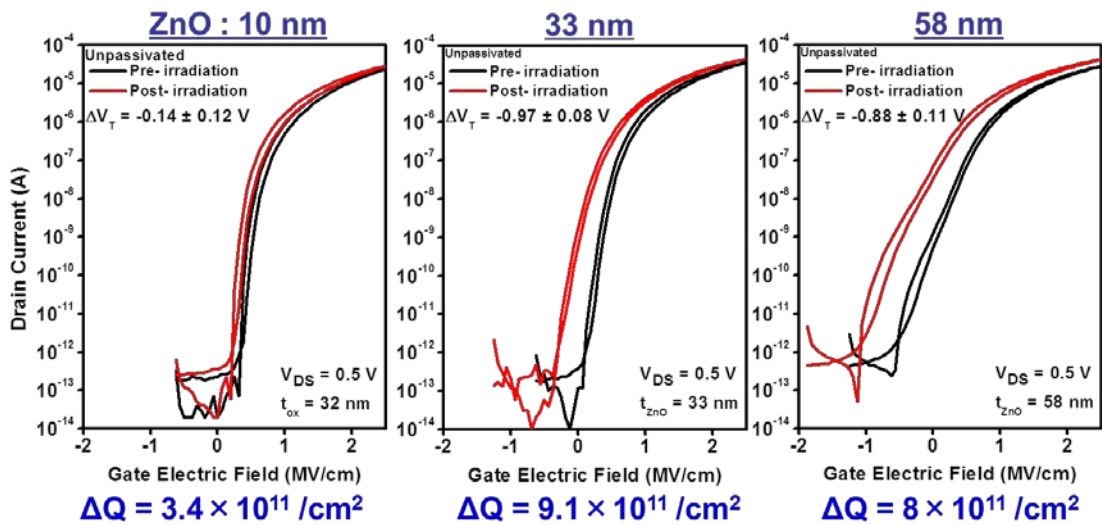


Figure 36. PEALD ZnO TFTs with active channel thicknesses and no passivation. ZnO film thickness variations result in some variation of radiation-induced charge.

Lastly, we examined the effects of gate dielectric thickness variation when exposed to gamma irradiation Figure 34 (right). Three different gate dielectric thicknesses were chosen: 16 nm, 33 nm and 58 nm, with a fixed 10-nm thick ZnO film and same ALD passivation. Figure 37 shows $\text{Log}(I_{DS})$ versus V_{GS} for ZnO TFTs with different gate dielectric thicknesses. The variation in gate dielectric thickness had negligible effects on the radiation-induced charge collected in the device after 5 Mrad suggesting negligible trapping in the bulk of the Al_2O_3 gate dielectric up to the thicknesses grown here.

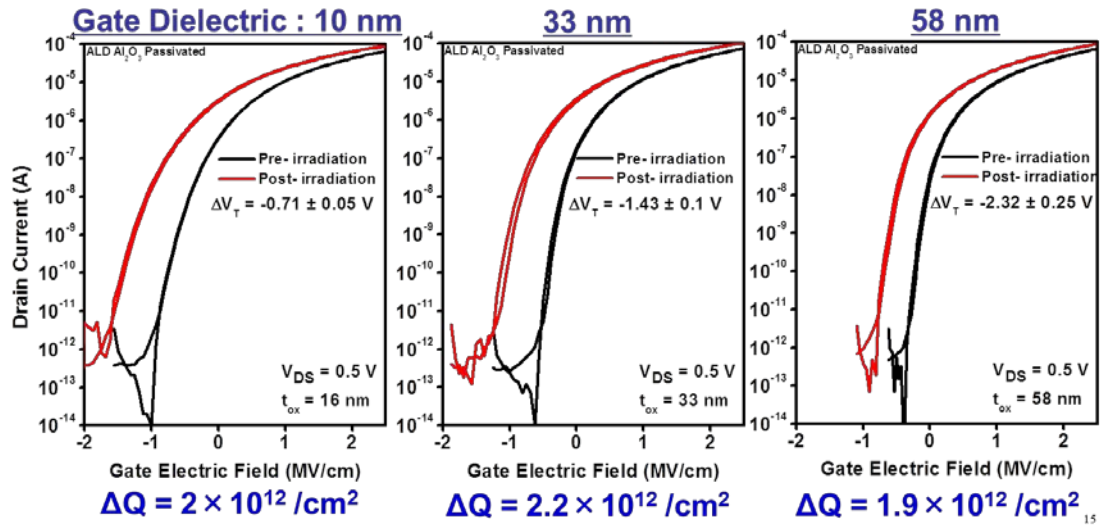


Figure 37. PEALD ZnO TFTs with varying gate dielectric thickness, fixed active channel thickness, and same ALD passivation. Gate dielectric thickness variations result in negligible change in charge for 5 Mrad dose.

To summarize and compare the changes in the different device permutations shown above we plotted V_{ON} and V_T shift as function of total film thickness stack for a cumulative dose of 5 Mrad, as shown in Figure 38. The V_{ON} shift is larger than V_T shift, particularly for thicker films. If the radiation-induced charge was captured by the bulk of the materials the V_{ON} shift would be similar to the V_T shift for all cases. The largest change observed for V_{ON} for pre-/post- irradiation was for passivated ZnO films indicated the passivation/ZnO interface dominates the radiation-induced charge collection in the device.

When all the device permutations are analyzed in terms of ΔQ , as shown in Figure 39, results show two clear groups of charged-induced on TFTs with passivation and without passivation. The active layer thickness variation with a passivation shows greatest ΔQ with irradiation. These results are consistent with a model that charge accumulation is at the ZnO/passivation interface. This charge can be modeled as sheet charge at this interface. Using the extracted ΔQ from this set of experiments we included them into our device modeling, shown in the modeling section.

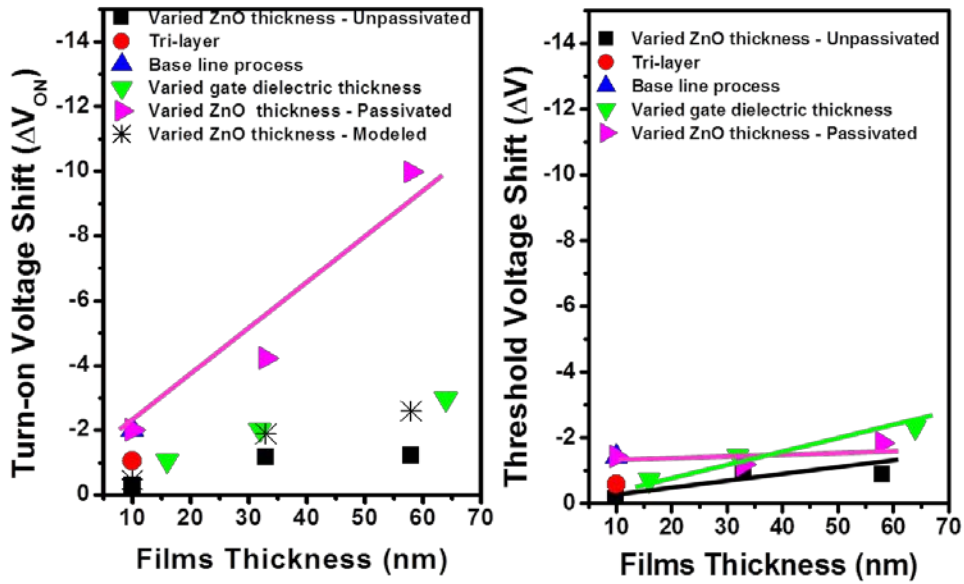


Figure 38. Summary of changes in V_{ON} (left) and V_T (right) as a function of process variants for TFTs exposed to 5 Mrad of ^{60}Co gamma radiation.

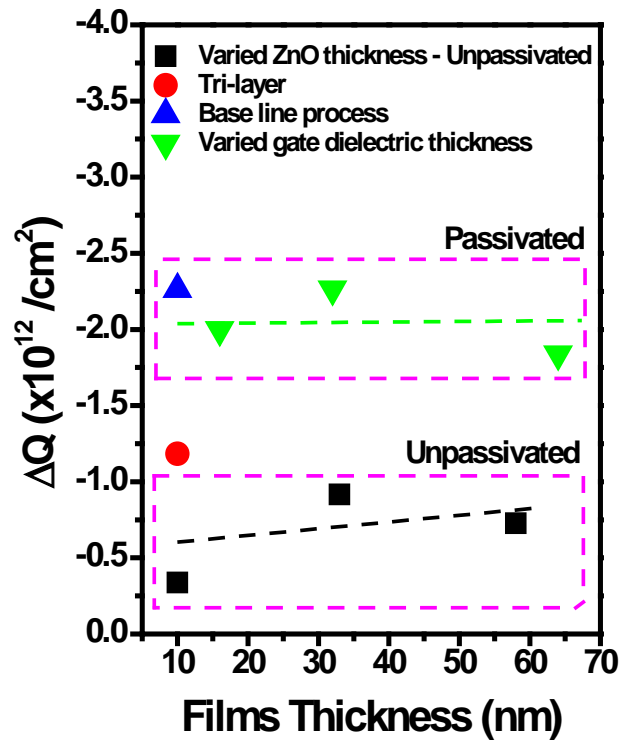


Figure 39. Summary of changes in charge as a function of process variants for TFTs exposed to 5 Mrad of ^{60}Co gamma radiation. The passivation/ZnO interface is most critical.

Materials Characterization and Defect Analysis

The major activities in the materials characterization and defect analysis work included grazing incidence x-ray diffraction (GIXRD), spectroscopic ellipsometry, and photoluminescence spectroscopy. The objectives of this task were to characterize the differences between ZnO films with similar crystallographic and electrical characteristics deposited by completely different techniques (PEALD and PLD) and to identify physical mechanisms for electrical degradation during irradiation and device recovery post-irradiation. A series of round robin experiments was conducted in which samples were prepared with both PLD and PEALD ZnO films and simultaneously subjected to the same gamma irradiation (20 Mrad ^{60}Co) and recovery conditions. The key outcome is the observation of spectroscopic differences in the samples as a function of growth and proposed physical mechanisms for unique defects observed in the materials. The observed defects validate the choice of parameters used in the Device Modeling section below in which different numbers of deep-levels and different density of states distributions give better physical models for device performance depending on the growth technique used.

Representative ZnO thin films deposited by PLD and PEALD, both 50 nm thick, were first characterized by GIXRD. The scans shown in Figure 40 highlight the similarity of the ZnO films used in this work independent of the growth technique. These results indicate both films are highly textured with a preferential (002) growth orientation. The intensity counts were normalized to facilitate comparison. Both films show a sharp intensity peak with a small full-width-half-maximum (FWHM). Coherence length is inversely proportional to FWHM and can be used to estimate crystal size. From the GIXRD, we observe similar grain size for both PEALD and PLD ZnO films.

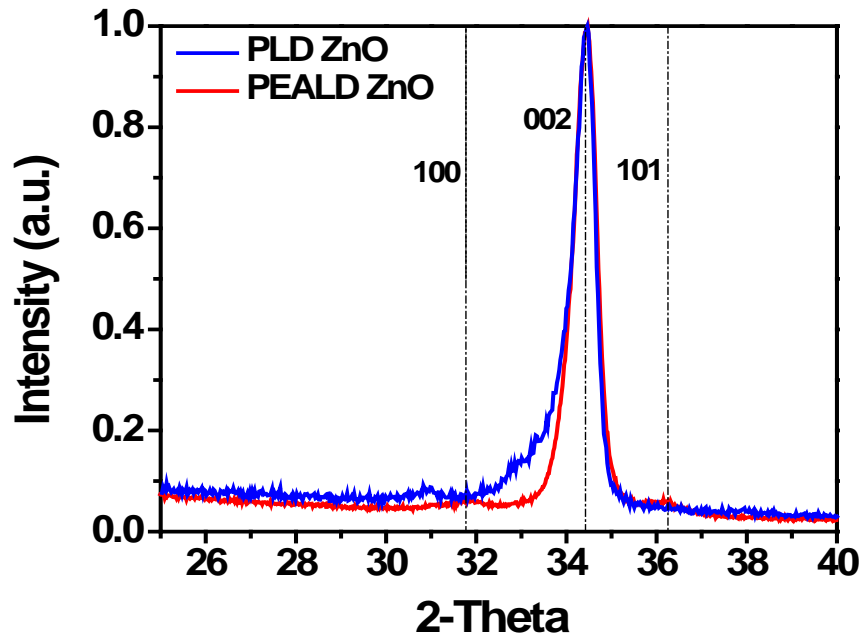


Figure 40. Grazing incidence XRD of ZnO thin films deposited by PLD and PEALD both show highly texture films with (002) orientation and coherence length suggesting similar grain size.

Spectroscopic ellipsometry was used to look for differences in optically active defects in the materials by measuring polarization of the material, ϵ_1 , as a function of photon energy. The second component of the complex dielectric function, $\epsilon = \epsilon_1 + i\epsilon_2$, the absorption coefficient, ϵ_2 , starts contributing to the dielectric functions when the ZnO material starts to absorb. The absorption coefficient, ϵ_2 , is extracted from the complex dielectric function, using parameterization. Comparing ϵ_2 for ZnO grown by PLD and PEALD, shown in Figure 41, indicate PLD-deposited ZnO has a sharper on-set absorption slope than ZnO PEALD. This suggests ZnO deposited by PEALD likely has a broader tail-state distribution than ZnO deposited by PLD. In the Device Modeling section, electrical characteristics of TFTs grown by PEALD were successfully modeled with a broader Gaussian distribution than TFTs grown by PLD.

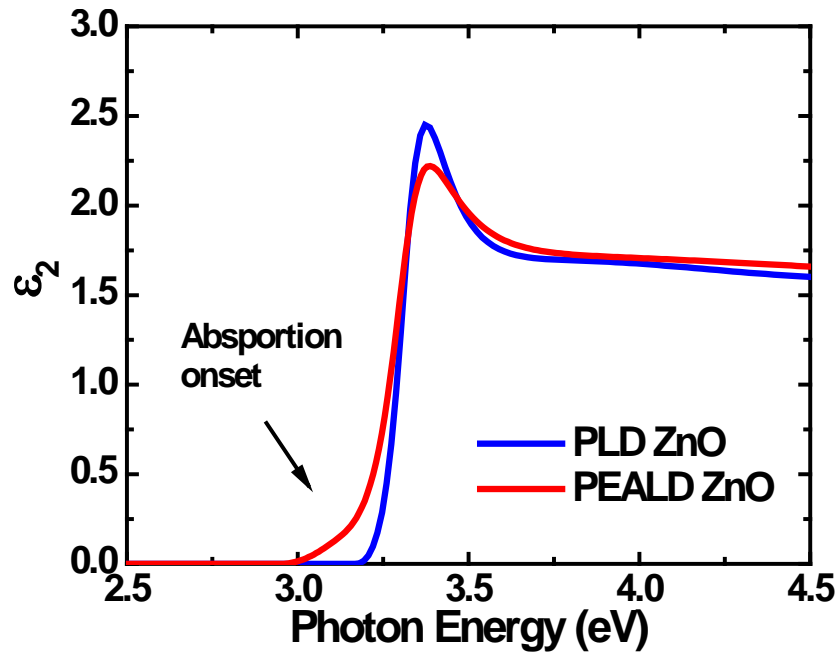


Figure 41. Absorption coefficient extracted by parameterization using spectroscopic ellipsometry. PEALD ZnO films has a slower absorption onset than PLD ZnO films suggesting a broader tail-state distribution for PEALD ZnO films.

Low-temperature photoluminescence spectroscopy (PLS) was used to measure the energy level of defects present in the materials as a function of device processing. Energy levels of photoemission from ZnO band-structure and defects are well documented in the literature and provide vital clues to the differences in the materials and ultimately physical mechanisms of radiation damage and self-healing properties. Expected defects common to both materials include Al donors due to low level impurities in gases ($<10^{16} \text{ cm}^{-3}$), native defects such as oxygen and zinc vacancies (V_O , V_{Zn}) and related complexes, and possibly cubic inclusions. Figure 42 and Figure 43 show expected calculated energy levels for point defects, both native and extrinsic, for ZnO materials. Of particular interest, are transitions associated with V_O that are known to produce emission anywhere from 2.0 eV – 2.2 eV, as well as V_{Zn} and Zn_O that can add to or shift observed mid-gap emission. Other important transitions to consider include nitrogen substitutional impurities and acceptors formed with N at around 120 and 170 meV above the valence band [45]. This is particularly important for the PEALD samples since they are grown by cracking N_2O molecules as the oxygen source for the ZnO materials. While N_2 molecules are interstitial impurities that are removed from the lattice during annealing, atomic N may form acceptor and deep level complexes in the lattice. Nitrogen substitutional impurities on an oxygen site (N_O) are known to be an

acceptor in ZnO and may form complexes with H. There is no nitrogen ambient in the PLD materials growth process. In all materials, we expect to see near bandedge emission (NBE) from donor bound excitons (D^0X_A) and possibly associated phonon processes as shown in Figure 44 along with deep level defect emission around mid-gap. Al-bound exciton emission is well known to occur at 3.36 eV.

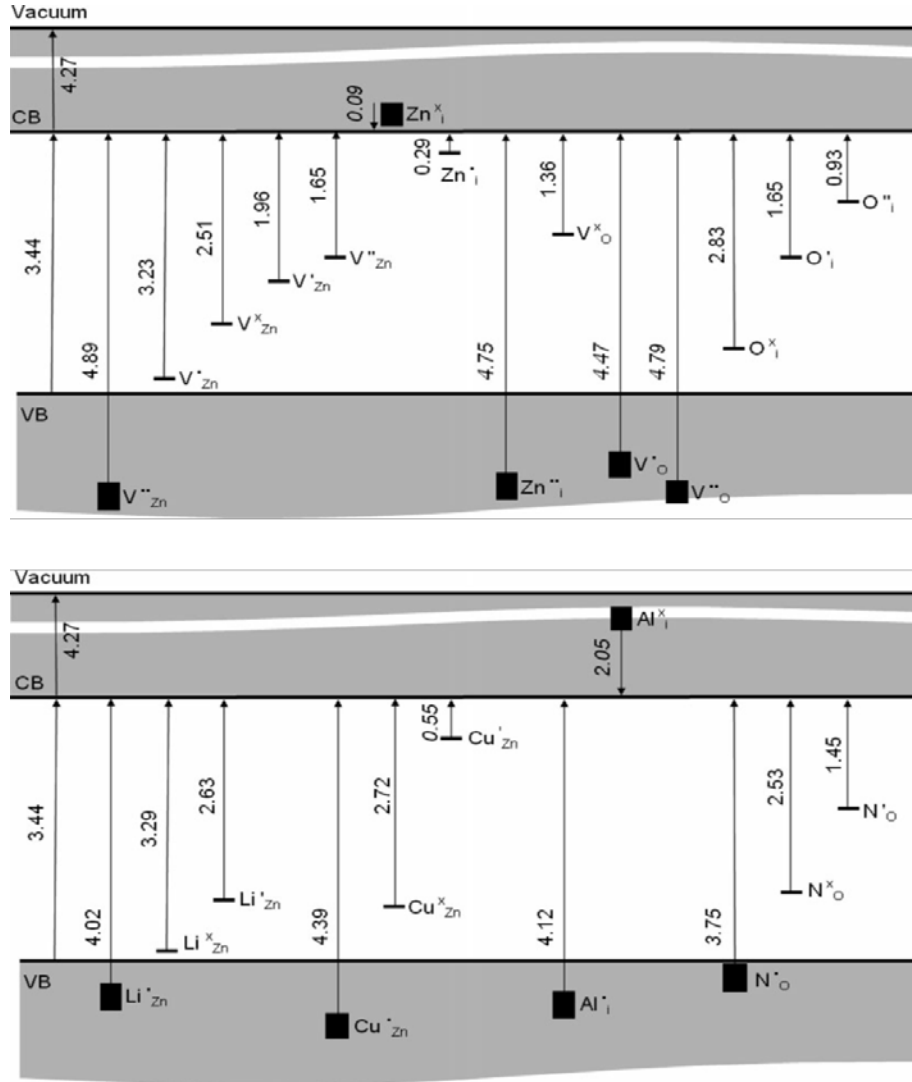


Figure 42. Donor defect levels in ZnO calculated by Sokol *et al.* [46] for native point defects on top and for extrinsic donor defects on bottom. Energy levels are shown with respect to the conduction band. Reprinted without permission.

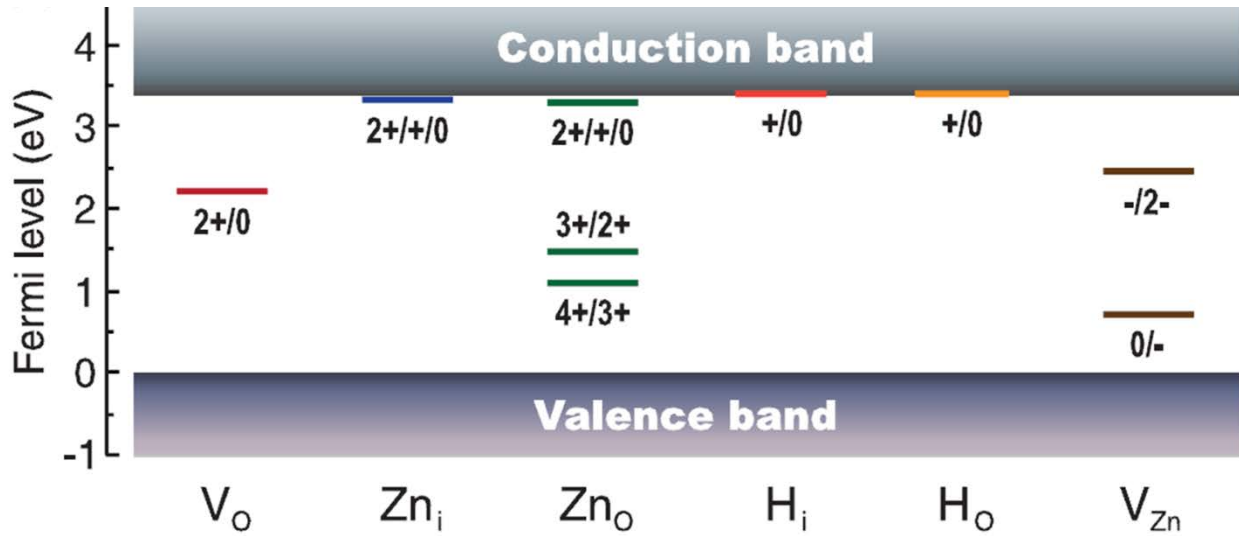


Figure 43. Energy levels for native and hydrogen point defects in ZnO calculated by Oba *et al.* [47]. Energy levels are calculated with respect to the valence band. Reprinted without permission.

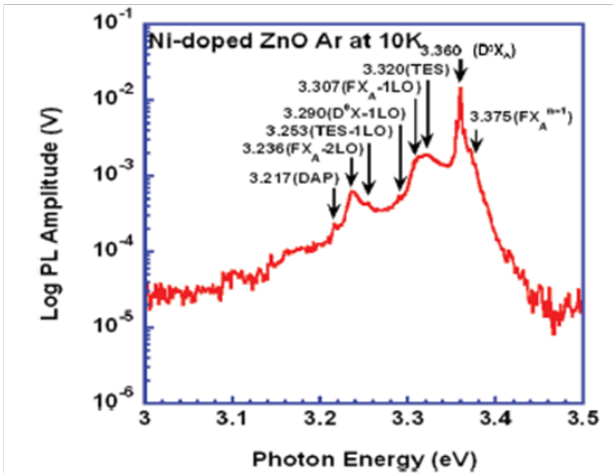
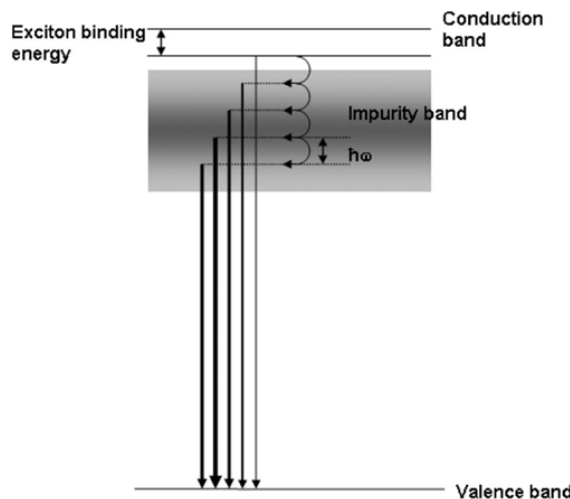


Figure 44. Left: Schematic showing phonon-assisted transitions in ZnO resulting in phonon-replica structures in PLS [48]. Right: Sample spectra at 10 K for Ni:ZnO films showing free-exciton, exciton, and phonon-assisted transitions [49]. Both reprinted without permission.

In this program, there were two rounds of sample exchanges in which thick and thin PLD and PEALD ZnO thin films were prepared and analyzed by PLS at 11 K 1) as grown, 2) after a 400 °C anneal and pre-irradiated, 3) post-irradiation (20 Mrad ^{60}Co), 4) after post-irradiation recovery anneal. The process flow for this experiment is shown in Figure 45. A composite plot of all PL spectra taken at 11 K for both PLD and PEALD grown samples as a function of processing and irradiation with ^{60}Co is shown in Figure 46. All PLD spectra are shown in red and all PEALD spectra are shown in black. Film thickness characterized for both PLD and PEALD materials are 10 nm and 50 nm. Though the plot is complex, we can make some general observations. Near-bandedge emission from Al-bound excitons at 3.36 eV was observed in all samples. Phonon replicas were observed near the bandedge in both types of materials but not all samples. This is expected for single crystal material, but somewhat surprising to observe in disordered material such as nanocrystalline ZnO and indicates high quality crystals. Expected mid-gap states were

observed in all materials peaking from 1.9 – 2.2 eV. These mid-gap states are attributed to transitions from an oxygen vacancy (V_O) to an acceptor or the valence band. The peak photon energy of the mid-gap distribution for PEALD materials occurs around 1.97 eV while the peak photon energy of the mid-gap distribution for PLD materials occurs 130 meV higher at 2.10 eV. PLD materials exhibit an additional mid-gap state with a low density of states around 2.55 eV. Some PEALD samples exhibit a defect pair at around 3.24 eV and 3.17 eV. Some PEALD samples exhibit a defect pair at around 3.24 eV and 3.17 eV.

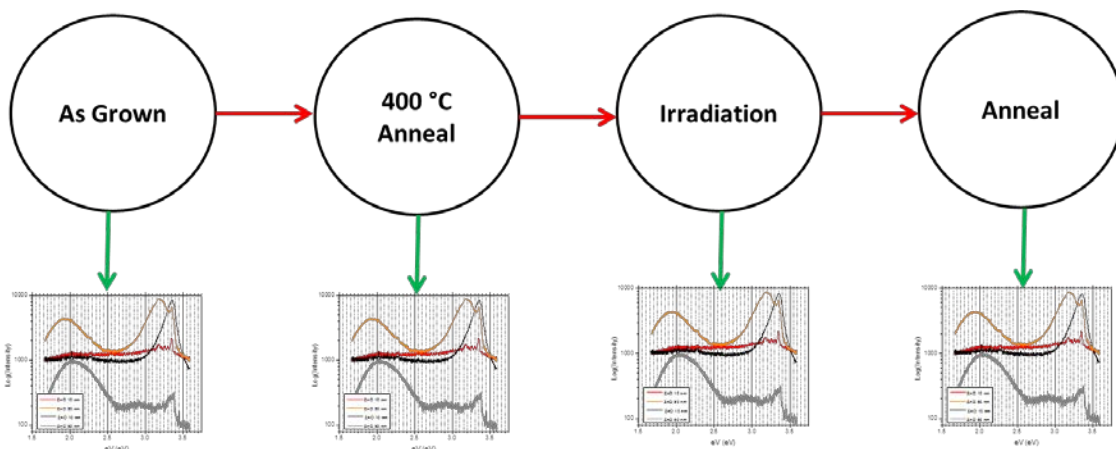


Figure 45. Process flow for PLS characterization of samples as grown, annealed, pre- and post-irradiation, and again after annealing is shown.

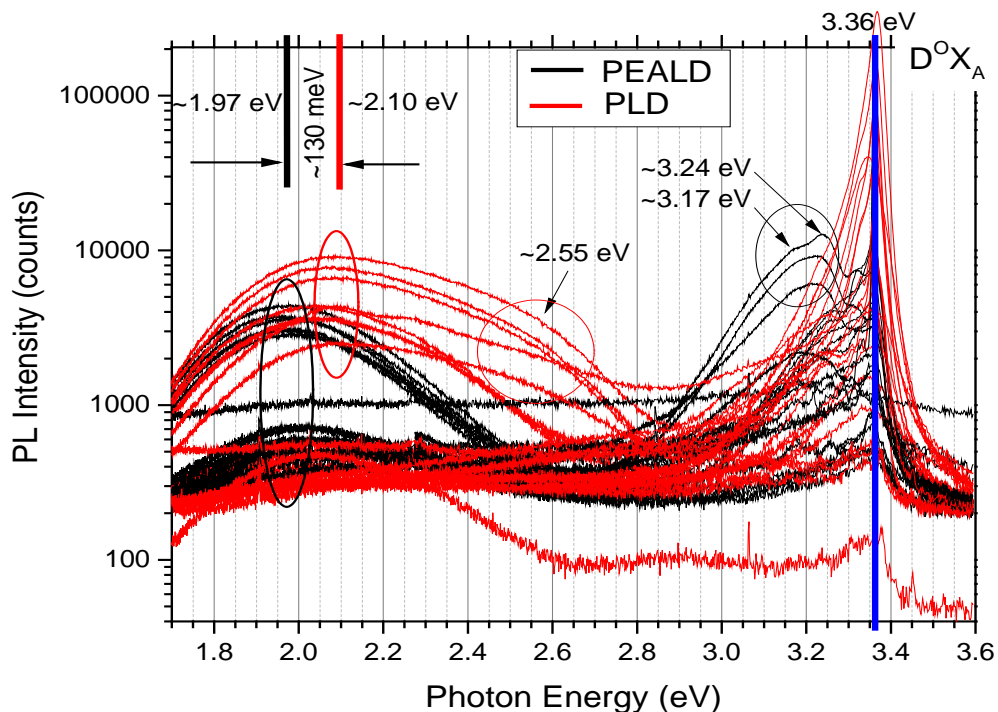


Figure 46. Composite plot of all PL spectra obtained at 11 K for both PEALD (black) and PLD (red) for all processing steps.

For clarity, we look in detail around the bandedge of PLD and PEALD films optimized for electrical performance. The PLD films are 50 nm and are baked at 400 °C after deposition. The PEALD films are 10 nm and do not have a 400 °C bake after deposition. Figure 47 shows the PL spectra for these films as prepared, after gamma irradiation, and after recovery bake. PLD films very clearly indicate donor-bound and free exciton (D^0X_A and FX_A) transitions as shown by Singh [49] as well as the two electron satellite (TES) transition. Both PLD and PEALD films show phonon replicas of the free exciton peak (FX_A -1LO and FX_A -2LO). PEALD films exhibit a unique pair of peaks at around 3.25 eV and 3.18 eV. This pair of peaks appear in several of the PEALD spectra and none of the PLD spectra. We tentatively assign this as a donor-acceptor pair (DAP) transition from the D^0X_A or FX_A to an acceptor state formed by a nitrogen substitutional impurity on an oxygen site (N_O).

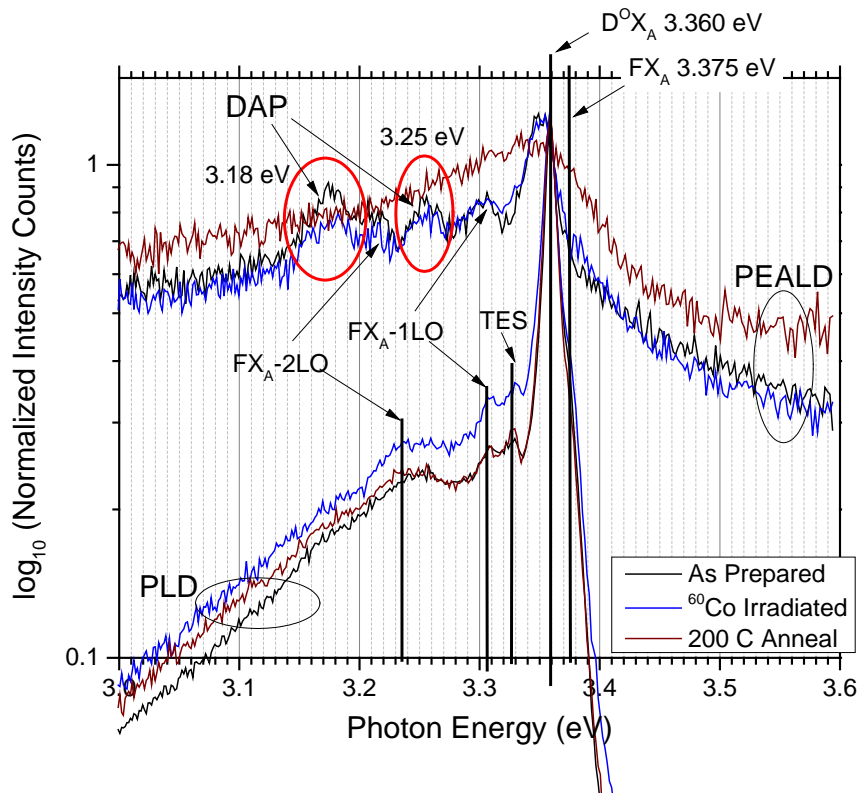


Figure 47. PL spectra for PEALD and PLD ZnO films optimized for electrical performance near the bandedge as a function of processing. Excitonic features and phonon replicas are evident in both materials. The PEALD films show a pair of peaks that are not phonon replicas and are assigned as donor-acceptor pair transitions.

It is important to note that the gamma irradiation does not have any impact on the fine structure of the PL spectra. This is the case in general and suggests that there is no effect due to atomic displacement within the ZnO film occurring during irradiation. Fine structure such as the DAP pairs and phonon replicas are strongly impacted by the 400 °C bake and 200 °C recovery bake. For samples that have not been baked at 400 °C prior to irradiation, the recovery bake does reduce or remove DAP peaks and phonon replicas. For samples that have been baked at 400 °C prior to irradiation, the recovery bake does not change the spectral features. This suggests that the bake drives out or changes bonds between

N_O and H, but gamma irradiation does not. Figure 48 clearly shows the impact of annealing on spectral features for samples that have been exposed to gamma radiation for 10 nm PEALD ZnO films. Figure 49 shows PL spectra for 50 nm PLD ZnO films treated with a 400 C anneal prior to irradiation.

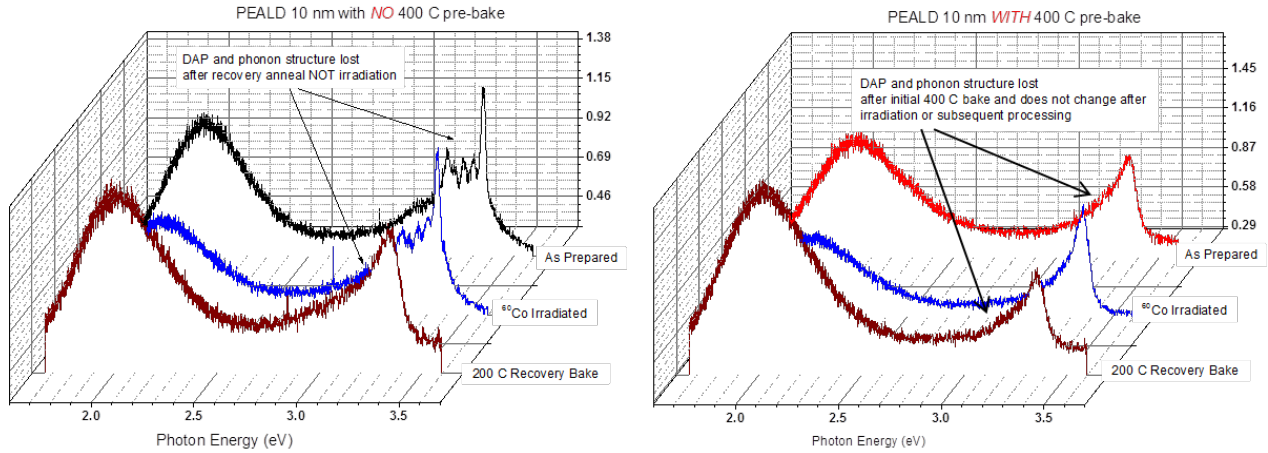


Figure 48. PL spectra for thin PEALD films as a function of irradiation and recovery anneal at 200 °C for as-deposited films (left) and films treated with a pre-bake at 400 °C (right). These spectra are normalized to NBE. Annealing causes spectral feature changes related to DAP and phonon processes while irradiation only changes relative intensity of the features.

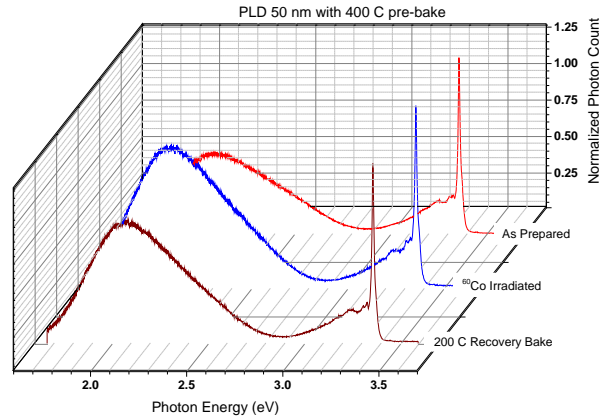


Figure 49. PL spectra for thick PLD films as a function of irradiation and recovery anneal at 200 °C for films treated with a 400 °C pre-bake at 400 °C. There is no change in the NBE and fine structure. Only relative intensity changes are observed.

Table 2 shows a summary of gaussian peak fits to the D^0X_A energy level and FWHM for PLD and PEALD films as prepared, after irradiation, and after recovery anneal. The change in energy level and FWHM after irradiation and recovery bake are tabulated. Changes in D^0X_A energy levels due to irradiation are all < 7 meV or within measurement error due to low signal and imperfect gaussian fit. Changes in D^0X_A FWHM are also within error. The sample with the highest signal to noise ratio and cleanest fit were the

50 nm PLD samples with the 400 °C bake. These samples exhibited > 0.9 meV shift in D^0X_A energy level and > 0.09 meV in FWHM after irradiation and recovery anneal at 200 °C. Gamma radiation did not measurably change defect spectroscopy structure or energy levels. The primary impact of gamma radiation was to change relative contributions of defect levels and bandedge emission.

Growth Method	Film Thickness	As Deposited	400 C Bake	Irradiated	Recovery Anneal 200 C	Exciton Peak (eV)	Exciton Peak Shift (meV)	FWHM (eV)	FWHM Change (meV)
PEALD	10 nm					3.34908		0.02958	
PEALD	10 nm					3.3487	-0.38	0.03071	1.13
PEALD	10 nm					3.34822	-0.48	0.09148	60.77
PEALD	10 nm					3.35071		0.09114	
PEALD	10 nm					3.3505	-0.21	0.07842	-12.72
PEALD	10 nm					3.352	1.5	0.09518	16.76
PEALD	50 nm					3.34989		0.06297	
PEALD	50 nm					3.34584	-4.05	0.06954	6.57
PEALD	50 nm					3.35216	6.32	0.0456	-23.94
PEALD	50 nm					3.35889		0.03279	
PEALD	50 nm					3.3545	-4.39	0.03949	6.7
PEALD	50 nm					3.35818	3.68	0.03079	-8.7
PLD	10 nm					3.34225		0.13904	
PLD	10 nm					3.34331	1.06	0.12079	-18.25
PLD	10 nm					3.35619	12.88	0.09915	-21.64
PLD	10 nm					3.36168		0.02095	
PLD	10 nm					3.36767	5.99	0.03739	16.44
PLD	10 nm					3.36354	-4.13	0.02327	-14.12
PLD	50 nm					3.34518		0.09502	
PLD	50 nm					3.3525	7.32	0.06576	-29.26
PLD	50 nm					3.35279	0.29	0.06671	0.95
PLD	50 nm					3.3592		0.01028	
PLD	50 nm					3.35836	-0.84	0.01034	0.06
PLD	50 nm					3.35874	0.38	0.01043	0.09

Table 2. Summary of donor bound exciton peak energy level and FWHM as a function of processing for thick and thin PEALD and PLD films. The change in peak energy level and FWHM are shown as a function of irradiation and recovery anneal for each sample.

A map of the most common transitions observed in both PLD and PEALD spectra is shown in Figure 50 with tentative assignment of physical cause. There is no doubt that the donor bound exciton is observed at 3.36 eV and that mid-gap states peaking from 1.9 – 2.2 eV are related to V_O transitions. We speculate that V_{Zn} is the cause of some of the spectral features observed in PLD films and have strong evidence to suggest that there is a DAP transition related to N_O observed in PEALD films. A N_O acceptor level could explain the observed peaks at 3.25 eV and 3.17 eV around the bandedge as well as the red-shift of about 130 meV in mid-gap emission with respect to PLD films which should have no N incorporation.

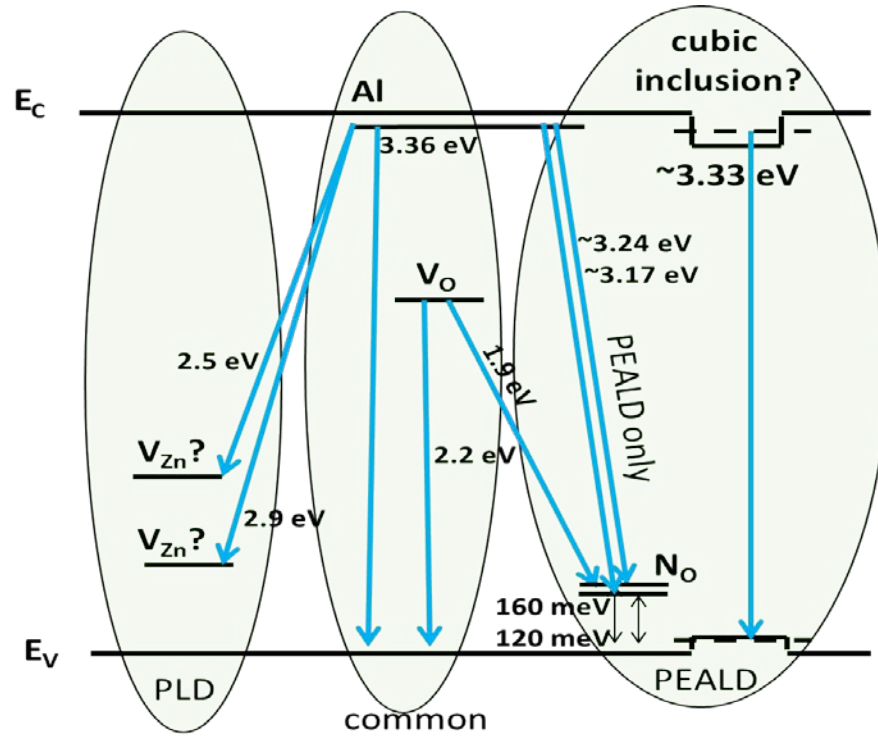


Figure 50. Band structure of observed states by PLS in ZnO. Transitions common to both materials are indicated in the center. Transitions observed only in PLD are on the left and transitions only observed in PEALD are on the right.

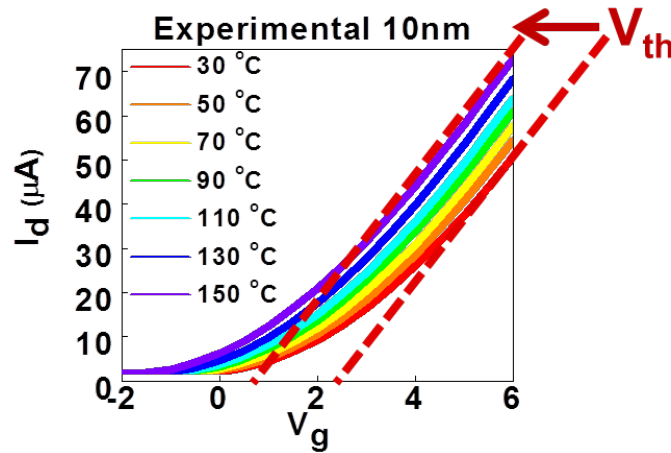
The outcome from the enhanced characterization effort is, for the first time, we have attempted to assign physical identification to observed spectral features and use this as input for Device Modeling efforts. Measured defect energy levels provided feedback to physical modeling activities in the next section in terms of improving initial guesses for defect energy levels and DOS for each level. Being able to observe the evolution of defect spectra as a function of processing and irradiation is a major advance in being able to understand the root physical causes of changes in electrical performance and self-healing in ZnO TFTs.

We show clearly that there is an additional state in PEALD materials that is not present in PLD materials. This observation is consistent with the need to model PEALD device performance with one more trap than PLD materials in the Device Modeling section. We also show that gamma irradiation does not produce any spectroscopically observable change in point defects. Changes in PL intensity due to irradiation are consistent with competing non-radiative recombination processes at the surface or an interface. This is consistent with the observations in the prior section showing that changes in charge are occurring primarily on the top surface of the ZnO film and successful modeling of the DC-IV curves by assuming a charge model at the ZnO/passivation interface. Substantial work remains in this area and it is necessary to follow up with additional radiation sources such as neutron irradiation and other characterization techniques to see if similar effects are observed. Overall, ZnO thin films appear extremely robust to irradiation, but must be thermally stabilized prior to use in a harsh environment.

Device Modeling

The goal for the device modeling was to first usefully model the as-fabricated PEALD and PLD TFTs and then extend the modeling to understand radiation-induced changes. The Synopsis Sentaurus Device simulator was used for this work. This software allows two- and three-dimensional modeling of multiple materials systems and device physics including electrical, thermal, and optical characteristics. Sentaurus Device is also capable of modeling single event effects and total ionization dose effects. To provide data to guide model development, ZnO TFT $I_D(V_G)$ curves were measured as a function of temperature as shown in Figure 51. The observed non-square-law behavior and V_T shift with temperature can be modeled using distributions of carrier traps near the conduction band minimum. The general model used includes two or three Gaussian trap distributions including a narrow distribution near the conduction band minimum (CBM) and a deep broad trap distribution.

Two-dimensional models were developed for both PEALD and PLD ZnO TFTs and the results indicated significant differences in the material properties. PEALD ZnO TFTs could be modeled as having intrinsic electron mobility (μ) of $50 \text{ cm}^2/\text{V}\cdot\text{s}$ with a very narrow, high-density trap distribution at the CBM ($\sigma = 0.005 \text{ eV}$, $N_0 = 1.5 \times 10^{21} \text{ cm}^{-3}$) and a very broad distribution of states centered around 0.5 eV below the CBM ($\sigma = 0.5 \text{ eV}$, $N_0 = 6 \times 10^{17} \text{ cm}^{-3}$). On the other hand, PLD ZnO TFTs could be modeled with a significantly higher mobility ($\mu = 200 \text{ cm}^2/\text{V}\cdot\text{s}$) with a wider, medium-density trap distribution at the CBM ($\sigma = 0.2 \text{ eV}$, $N_0 = 1.5 \times 10^{18} \text{ cm}^{-3}$) and no mid-gap states. A comparison of the trap levels and density is shown in Figure 52.



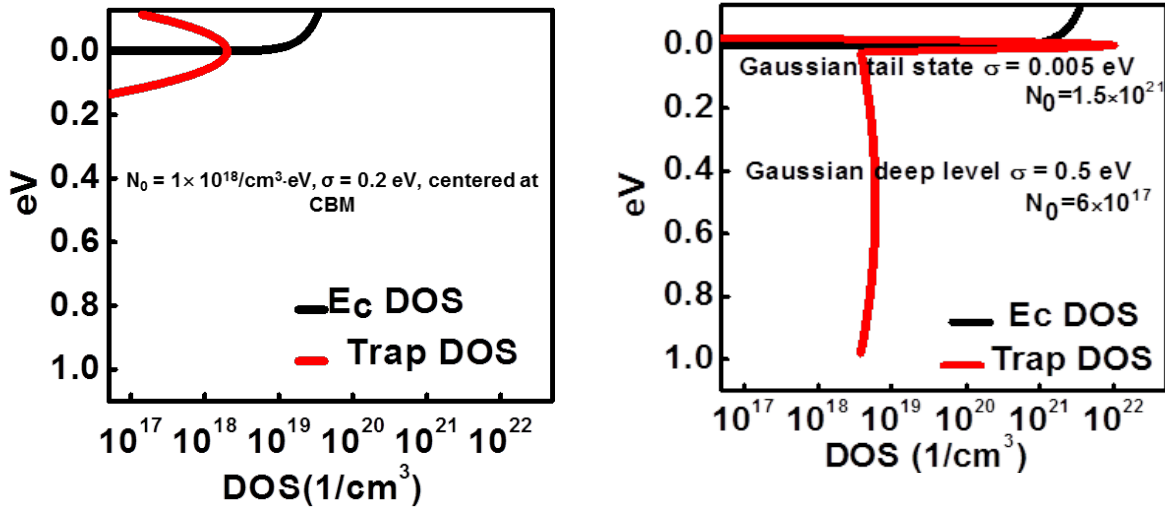


Figure 52. Trap density and distribution comparison between PLD ZnO TFTs (LEFT) and PEALD ZnO TFTs (RIGHT). PLD grown TFTs exhibit behavior consistent with higher mobility and negligible mid-gap states. PEALD grown TFTs are better fit with lower mobility and higher trap density of states at the CBM and mid-gap.

The model requirement of additional trap states to fit the PEALD TFT characteristics compared to PLD TFTs is in general agreement with the material characterization results for PEALD and PLD ZnO. However, the material characterization also suggested traps with energy deeper into the forbidden band were also likely. Also, because many of the PEALD TFTs used in this study were fabricated on low thermal conductivity glass substrates, the device testing was extended to pulsed measurements to eliminate self-heating effects. The goal was to self-consistently model a wide range of device characteristics, including the shape of the linear drain current versus gate voltage (I_d versus V_g) characteristics, the temperature dependent drain current versus gate voltage, temperature dependent quasi-static capacitance-voltage (QSCV) measurements, the drain current versus drain bias characteristics, transmission line measurements (TLM), and characteristics of devices with thickness variations.

Synopsys TCAD Sentaurus Device was again used for two-dimensional device simulations. An example device structure for simulation is shown in Figure 53 (left). Transient simulations were used to fit quasi-static capacitance-voltage data and quasi-stationary simulations to fit all other experimental data. The basic simulation parameters are summarized in Table 3. Simulations with only these parameters did not fit the experimentally observed data (threshold voltage shift with temperature, slow ramp quasi-static capacitance-voltage overshoot). To fit the experimental data we added trap distributions near the ZnO conduction band edge and also a small barrier at the contacts.

Approximately 500 simulation runs were done to optimize the trap distributions and contact barrier. The best fit was found for one Gaussian trap distribution centered at the conduction band minimum with peak of $2 \times 10^{22}/\text{cm}^3\text{-eV}$ and $\sigma = 0.005$ eV and a second Gaussian trap distribution centered 0.5 eV below the conduction band minimum with peak of $6 \times 10^{18}/\text{cm}^3\text{-eV}$ and $\sigma = 0.5$ eV. The trap density is assumed to be uniform throughout the active layer. Figure 53 (right) shows the trap distributions. The simulations also included a contact barrier of 0.1 eV, with barrier tunneling included in the simulation physics.

ZnO parameters	
Bandgap	3.37 eV
Electron affinity	4.1 eV
Electron mobility	200 $\text{cm}^2/\text{V}\cdot\text{s}$
Contact barrier	0.1 eV
E_c DOS	$3.66 \times 10^{18}/\text{cm}^3$
Electron tunneling mess	0.5 m_0
Dielectric constant	8

Table 3. Modeling parameters used in Sentaurus Device for ZnO TFTs.

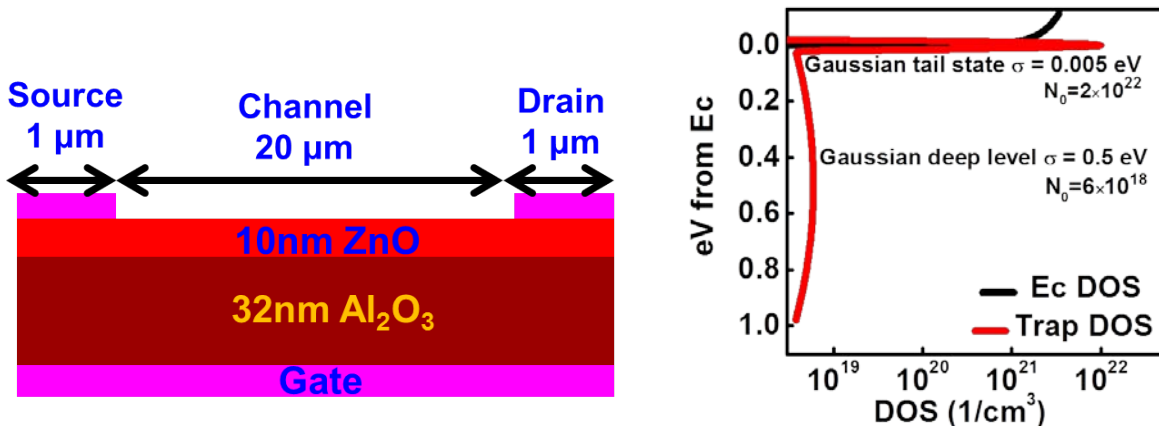


Figure 53. (Left) Example device structure for simulation. (Right) Initial trap distribution optimization.

Although the trap distributions described above were successful in qualitatively fitting the temperature dependent I-V characteristics, the trap densities required also resulted in a sub-threshold slope larger than experimentally observed. Experimental sub-threshold slope for PEALD TFTs varies somewhat with device structure and processing, but is typically 80 - 250 mV/decade. Using the trap distribution from above, the simulated sub-threshold slope is 370 mV/decade.

After carefully revisiting the big difference in subthreshold slope between the simulated and experimental result, we realized that self-heating can complicate experimental measurements. Because PEALD ZnO TFTs are typically fabricated on low-thermal-conductivity substrates (glass) even mW power levels typically used in device testing can cause significant device self-heating. This means that in our variable temperature I-V measurements, the temperature depends not only on the sample fixture temperature, but also on the device input power.

To eliminate this effect, we repeated our experimental measurements using short duration (< 1 ms), low duty cycle ($< 2\%$) pulses. Figure 54 shows temperature dependent I-V measurements using normal near-DC sweeps (left) and pulsed measurements (right). The temperature dependent shift is significantly reduced for the pulsed measurements.

We are able to fit the pulsed experimental data with significantly lower trap density. The best fit was found for one Gaussian trap distribution centered at the conduction band minimum with peak of $1.5 \times 10^{22}/\text{cm}^3\text{-eV}$ (3/4 of the trap density required with self-heating) and $\sigma = 0.005$ eV and a second Gaussian trap distribution centered 0.4 eV below the conduction band minimum with peak of $6 \times 10^{17}/\text{cm}^3\text{-eV}$ and $\sigma = 0.5$ eV (1/10 of the trap density required with self-heating). The simulations again included a contact barrier of 0.1 eV.

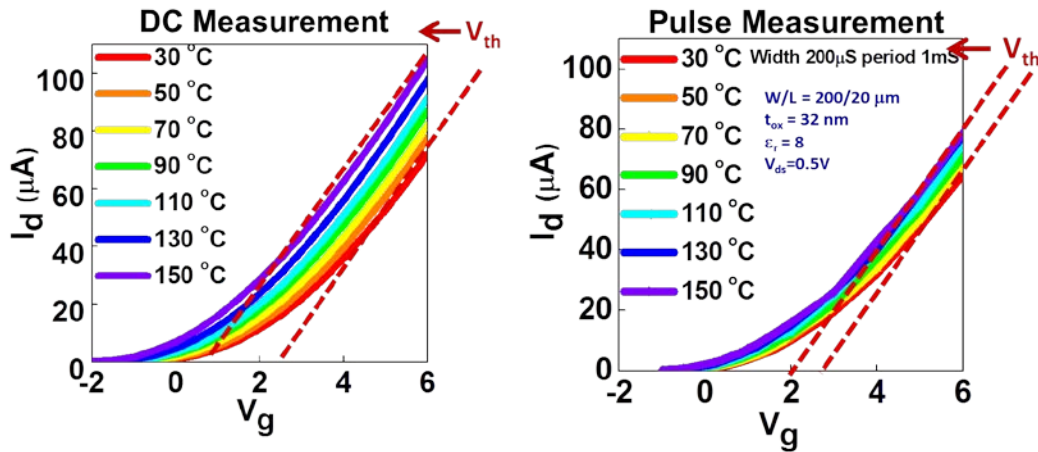


Figure 54. (Left) Nearly-DC sweeps as function of temperature I_{DS} - V_{GS} and (Right) Pulsed measured I_{DS} - V_{GS} . V_T spread is greater in DC measurements because of self-heating.

We have also simulated ZnO PLD devices. Because these devices are fabricated on silicon substrates with large thermal conductivity, pulsed and near-DC sweep measurements are very similar except at very large device power. Again, we are able to get a reasonable qualitative fit between simulation and experiment, however only a single trap distribution is required. The best fit was found for a single Gaussian trap distribution centered at the conduction band minimum with peak of $10^{18}/\text{cm}^3\text{-eV}$ and $\sigma = 0.2$ eV (again a contact barrier of 0.1 eV was used).

Because the simulation approach uses a constant mobility ($200 \text{ cm}^2/\text{V}\cdot\text{s}$), with traps used to match the experimental curves, it is expected that PLD ZnO devices would have a lower integrated trap density. It is interesting that the distribution details are also different. Notably, the photoluminescence data shows a peak below the bandgap energy for the PEALD ZnO devices, but not for the PLD ZnO devices, consistent with the two trap distributions required to fit PEALD ZnO devices and only one distribution required for PLD ZnO devices.

Although bulk trap distributions were used to fit the experimental data, the fit is not unique and we can fit the data about as well using traps localized at the ZnO/gate-dielectric interface. In principle, it should be possible to separate bulk and interface traps using data from TFTs with different active layer thickness. This analysis is complicated by the source-drain contact barriers. We have designed and fabricated TFTs with extra gates used to turn on the device contact regions and reduce contact effects. Results for these devices are better matched by bulk traps than by interface traps.

In addition to the uniform bulk trap distribution in the modeling described above the ZnO material was also treated as homogeneous. However, both PEALD and PLD ZnO films have a nanocrystalline microstructure. To consider microstructure effects we implemented a model for grain boundaries into our simulations.

Because grain boundaries are three-dimensional structures requiring complex and time-consuming modeling, we used a simplified two-dimensional structure as a first iteration. Figure 55 (left) shows an example modeled device structure. In this example structure the grain size is 50 nm. A constant mobility of $200 \text{ cm}^2/\text{V}\cdot\text{s}$ is used inside the grains and $50 \text{ cm}^2/\text{V}\cdot\text{s}$ is used in a 1 nm wide region at the grain boundary. Traps are included only at the grain boundaries and barrier tunneling is also included near the grain boundaries. A rough optimization found a best fit to the experimental data using two trap distributions: a Gaussian distribution centered at the conduction band minimum with peak of $4 \times 10^{22} / \text{cm}^3\cdot\text{eV}$ and $\sigma = 0.005$ and a second Gaussian distribution with peak of $5 \times 10^{19} / \text{cm}^3\cdot\text{eV}$ and $\sigma = 0.5$ centered about 0.5 eV below the conduction band minimum, Figure 55 (right).

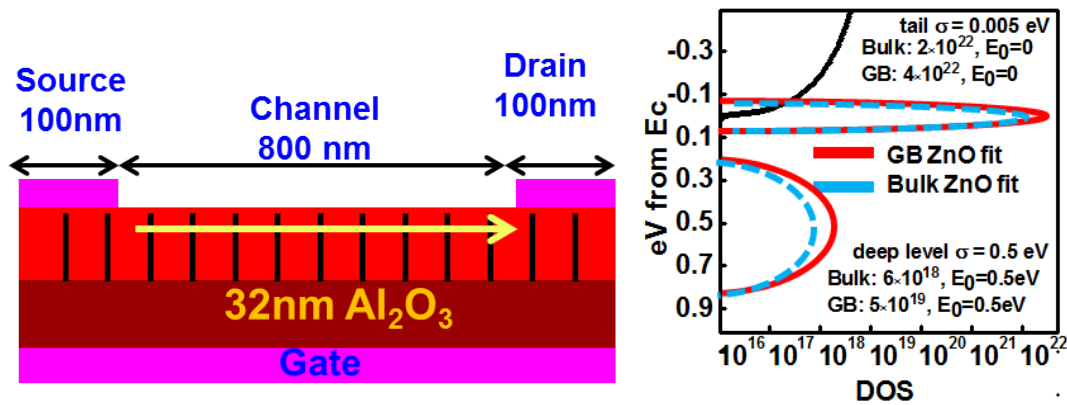


Figure 55. (Left) Two-dimensional grain boundary model example, (right) grain boundary confined trap distribution.

The simplified two-dimensional grain boundary modeling showed that a relatively high density of grain boundaries with a large local trap density can give simulation results that qualitatively match the experimental results, similar to the simple bulk trap (no grain boundaries) approach. However, the two models are not the same because the grain boundary model depends not only on the trap density, but also on the grain boundary density. Figure 56 shows the grain boundary related barriers (top row of plots) along the TFT channel (along the arrow in Figure 55 (left)) for different numbers of grain boundaries and varying grain boundary spacing. Figure 56 (bottom row of plots) shows the resulting drain current as a function of gate bias and temperature. The most noticeable effect is an increase in current with a decrease in the number of grain boundaries.

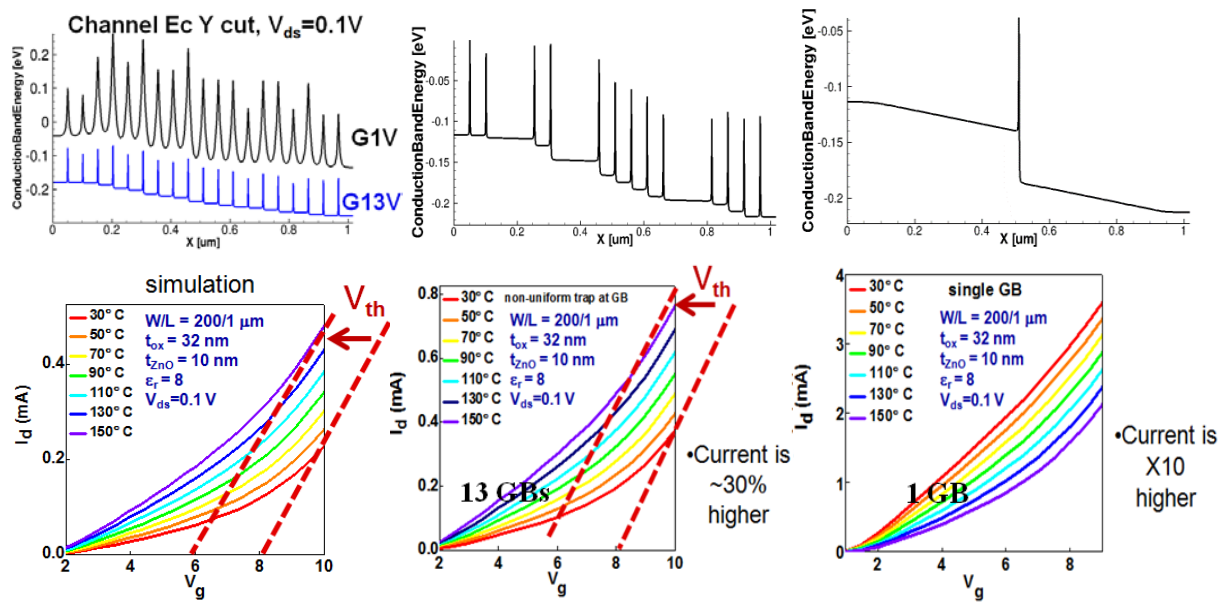


Figure 56. (Top row) Grain-boundary related barrier along TFT channel. (Bottom row) Drain current as a function of gate bias and temperature, both for varying numbers of grain boundaries.

The two-dimensional grain boundary modeling is interesting, but may be oversimplified to the point of limited utility. This is because in a real device grain boundary effects are unlikely to be isotropic. That is, in most models of grain boundary associated traps, the trap density depends on the local disorder or other effects at the grain boundary. Qualitatively this is like an obstacle course with a large number of wall-like barricades that vary widely in height with position. In running the obstacle course one would not be forced to go in a straight line and so would naturally choose to go over the low-height barriers. So the effect of the barriers would be both requiring the energy to surmount some height and also the work to zig-zag to find low barriers, running farther than a straight line path. This is similar to Hosono's distribution of above band edge barriers model [50], but with the possibility of improved connection to microstructure.

Modeling grain boundaries in this way requires three dimensions. Three dimensional modeling is more difficult because the number of mesh elements required is greatly increased and also because solution convergence can be more difficult. In addition, connection between microstructure and grain boundary traps or other effects is uncertain or unknown. Figure 57 (left) is a reminder of the columnar grain structure in PEALD ZnO thin films and (right) is an example simplified device structure with grain boundaries we have used in our three-dimensional modeling. Initial three-dimensional modeling indicated a wide range of parameters that can be used to qualitatively match device experimental characteristics.

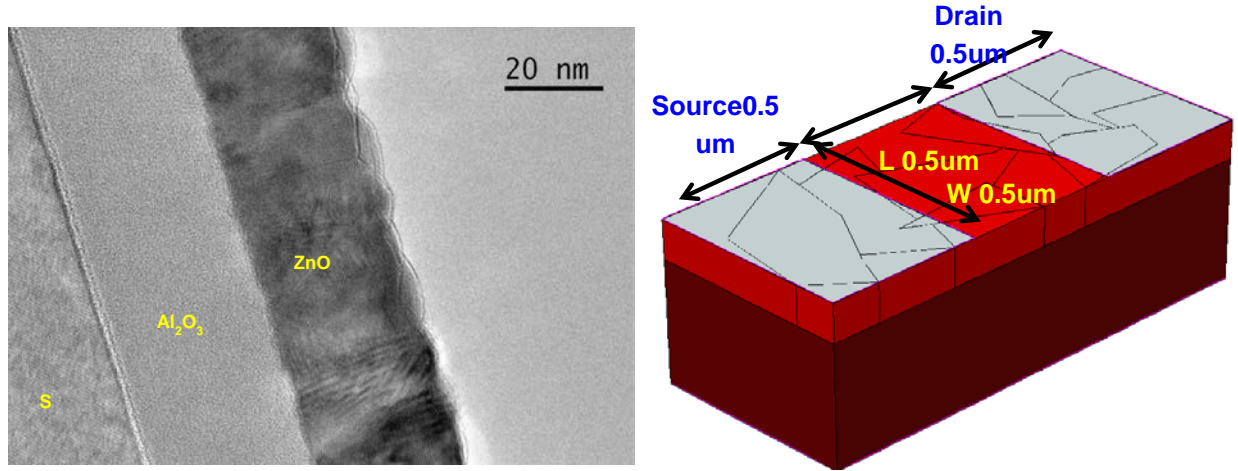


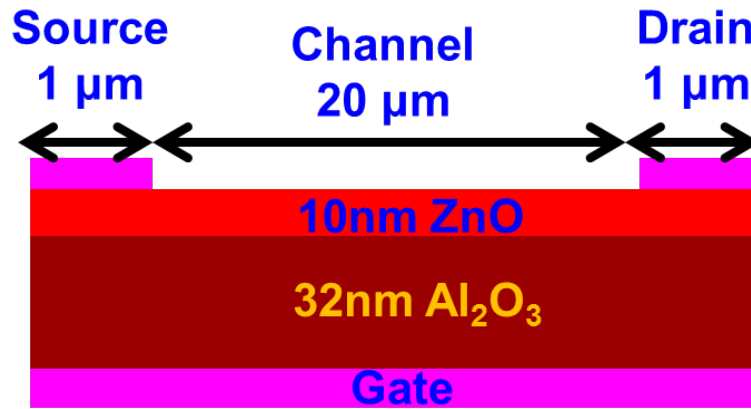
Figure 57. LEFT - Cross-sectional TEM of PEALD ZnO film. Right - TCAD Sentaurus 3D simulation structure.

Modeling of Radiation Induced Changes

A goal for the device modeling was to assist in understanding in ZnO TFTS. As described above, gamma ray irradiation produced shifts in the ZnO TFT I-V characteristics. Notably, the shift in turn-on voltage was larger than the shift in threshold voltage, with little change in mobility, but with strong effects related to passivation of the TFT back interface. Similar results have been observed by Mourey, et al, for passivation of ZnO TFT and were modeled as a charge sheet at the ZnO passivation interface [44]. A similar approach was used to model the radiation induced TFT changes. As a first step the trap distributions for the PEALD and PLD ZnO TFTs were refined to better fit the experimental characteristics. Figure 58 shows the modeled structure, general modeling parameters, and trap distributions used for the radiation induced TFT changes simulations.

PEALD ZnO TFTs with ZnO active layer thicknesses of 10, 30, and 50 nm were modeled. To match the experimental results, a positive sheet charge of 1.5×10^{12} electronic charges/cm² was introduced at the ZnO back interface (Figure 59 (top)). Figure 59 (bottom) shows the results. Notably, a single density sheet charge ($+1.5 \times 10^{12}$ electronic charges/cm²) does a good job of fitting the experimental characteristics for all three ZnO active layer thicknesses.

The device modeling confirms the importance of the ZnO TFT back interface or passivation interface for radiation-induced device changes. To further examine this, preliminary characterization of radiation exposure effects on an alternative, trilayer, PEALD ZnO TFT structure were done. For these PEALD ZnO TFTs the bottom dielectric layer, active ZnO layer, and top passivation layer are all deposited in sequence [51]. These TFTs have reduced passivation-induced device changes compared to the PEALD ZnO TFTs described earlier. Notably, the radiation induced changes for the trilayer PEALD ZnO TFTs were reduced compared to the standard device structure. This indicates that optimization of the ZnO TFT structure may allow minimization of radiation induced device changes.



PSU Baseline modeled structure

ZnO parameters	
Bandgap	3.37 eV
Electron affinity	4.1 eV
E_c effective DOS	$3.66 \times 10^{18} / \text{cm}^3$
Electron tunneling mess	$0.5 m_0$
Dielectric constant	8

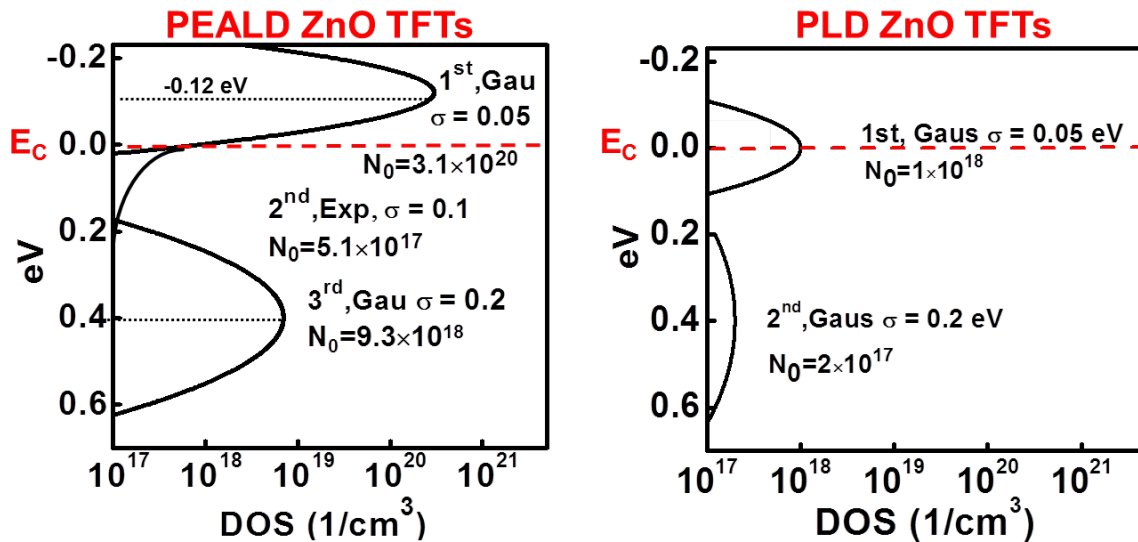


Figure 58. Modeled structure, general modeling parameters, and trap distributions used for the radiation induced TFT changes simulations in Electrical Characterization section for determination of physical location of changes induced by ^{60}Co gamma irradiation.

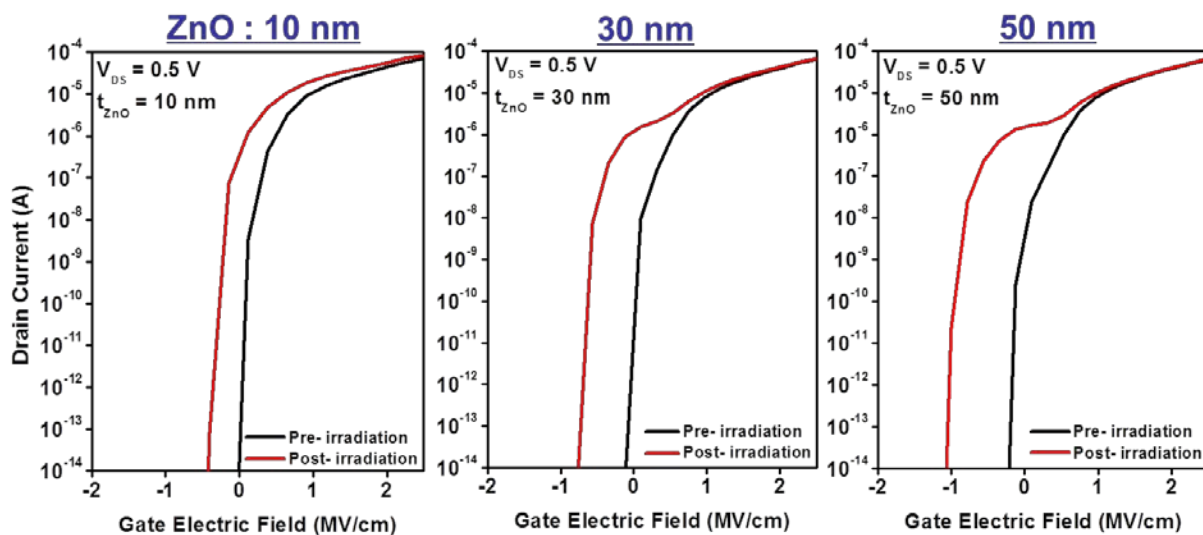
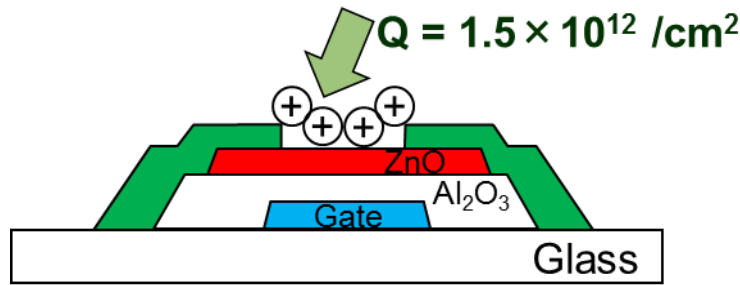


Figure 59. Cross-section of TFT modeled during exposure to ^{60}Co gamma irradiation as a function of ZnO active layer thickness variation in Electrical Characterization section. Predicted I-V curves describe the empirically observed change in threshold voltage as a function of thickness.

Summary

ZnO TFTs were found to have a high tolerance to gamma and neutron radiation for doses up to 100 Mrad. After removing measurement artifacts and charging during in-situ measurements, it was determined that in-situ biasing degradation mechanisms were similar to degradation seen without in-situ biasing. Spectroscopic measurements suggest the possibility of O and Zn vacancies in PLD ZnO materials and N substitutional impurities in PEALD ZnO materials. The largest factor affecting device performance changes due to irradiation appear to be the passivation/ZnO interface while the ZnO itself appears to be robust. Final simulation results are able to replicate shifts in V_T based on these new observations, quantifying charge changes due to irradiation at the top device interface. Significant work remains to optimize device structures for stability and passivation at the top ZnO interface, but the technology shows great promise for applications requiring rad-hard operation.

Bibliography

- [1] H. J. Barnaby, "Total ionizing dose effects in modern CMOS technologies," *IEEE Transactions on Nuclear Science*, vol. 53, pp. 3103 - 3121, 2006.
- [2] M. Papastamatiou, N. Arpatzanis, G. J. Papaioannou and A. Christou, "Neutron Radiation Effects in High Electron Mobility Transistors," *IEEE Transactions on Electron Devices*, vol. 44, pp. 364 - 372, 1997.
- [3] E. J. Kennedy, G. T. Alley, C. L. Britton Jr., P. L. Skubic, B. Gray and A. Wu, "Radiation effects on JFET MOSFETS and BJT as related to SSC circuit design," *Nuclear Instruments and Methods in Physics Research Section A: Accelerators, Spectrometers, Detectors and Associated Equipment*, vol. 307, pp. 452 - 457, 1991.
- [4] D. M. Li, Z. H. Wang, L. Y. Huangfu and Q. J. Gou, "Study of Total ionizing dose radiation effects on enclosed gate transistors in a commercial CMOS Technology," *Chinese Physics*, vol. 16, pp. 3760 - 3765, 2007.
- [5] W. C. Jenkins and S. T. Liu, "Radiation response of fully depleted MOS Transistor Fabricated in SIMOX," *IEEE Transactions on Nuclear Science*, vol. 41, pp. 2317 - 2321, 1994.
- [6] H. L. Hughes and J. M. Benedetto, "Radiation effects and hardening of MOS technology: Devices and Circuits," *IEEE Transactions on Nuclear Science*, vol. 50, pp. 501 - 521, 2003.
- [7] F. W. Sexton and J. R. Schwank, "Correlation of radiation effects in transistors and integrated circuits," *IEEE Transactions on Nuclear Science*, vol. 32, pp. 3975 - 3981, 1985.
- [8] J. W. Gambles, K. J. Hass and S. R. Whitaker, "Radiation hardness of Ultra Low Power CMOS VLSI," *11th NASA Symposium on VLSI Design*, 2003.
- [9] Y.-K. Moon, D.-Y. Moon, S. Lee and J.-W. Park, "Effects of high-dose proton irradiation on ZnO thin-film transistors," *Journal of the Korean Physical Society*, vol. 54, no. 3, p. 1059, 2009.
- [10] M. A. Xapsos, G. P. Summers and E. M. Jackson, "Enhanced total ionizing dose tolerance of bulk CMOS transistors fabricated for ultra-low power applications," *IEEE Transactions on Nuclear Science*, vol. 46, pp. 1697 - 1701, 1999.
- [11] V. Davidovic, D. N. Kouvatsos, N. Stojadinovic and A. T. Voutsas, "Influence of polysilicon film thickness on radiation response of advanced excimer laser annealed polycrystalline silicon thin film transistors," *Microelectronics Reliability*, vol. 47, pp. 1841 - 1845, 2007.
- [12] A. Pikor and E. M. Reiss, "Radiation-hardened CMOS integrated circuits," *Microelectronics Journal*, vol. 11, no. 4, pp. 27 - 30, 1980.
- [13] N. A. Hastas, C. A. Dimitriadis, J. Brini, G. Kamarinos, V. K. Guerguiev and S. Kaschieva, "Effects of gamma-ray irradiation on polycrystalline silicon thin-film transistors," *Microelectronics Reliability*, vol. 43, pp. 57 - 60, 2003.

- [14] C. K. Yang, C. L. Lee, T. F. Fei and H. N. Chern, "Radiation effects on n-channel polycrystalline silicon thin-film transistors," *Applied Physics Letters*, vol. 67, no. 23, 1995.
- [15] C. C. Foster, "Total ionizing dose and displacement-damage effects in microelectronics," *MRS Bulletin*, vol. 28, pp. 136 - 140, 2003.
- [16] I. S. Esqueda, H. J. Barnaby, K. E. Holbert, F. El-Mamouni and R. D. Schrimpf, "Modeling of Ionizing Radiation-induced Degradation in Multiple Gate FETs," *IEEE Transactions on Nuclear Science*, vol. 58, pp. 499 - 505, 2011.
- [17] Y. Wang, Z. Yan, J. Zhu, L. Zhang, X. Lin, J. He, J. Cao and M. Chan, "A generic numerical model for detection of terahertz radiation in MOS," *Solid-State Electronics*, vol. 54, no. 8, pp. 791 - 795, 2010.
- [18] A. M. Phanse, J. S. Yuan, C. S. Yeh and B. Gadepally, "Modeling the BiCMOS switching delay including radiation effect," *IEE Proceedings Circuits, Devices & Systems*, vol. 144, pp. 53 - 59, 1997.
- [19] H. J. Barnaby, S. K. Smith, R. D. Schrimpf, M. Fleetwood and R. L. Pease, "Analytical Model for Proton Radiation Effects in Bipolar Devices," *IEEE Transactions on Nuclear Science*, vol. 49, pp. 2643 - 2649, 2002.
- [20] V. V. Belyakov, A. I. Chumakov, A. Y. Nikiforov, V. S. Pershenkov, P. K. Skorobogatov and A. V. Sogoyan, "IC's radiation effects modeling and estimation," *Microelectronics Reliability*, vol. 40, pp. 1997 - 2018, 2000.
- [21] D. M. Fleetwood, P. S. Winokur, L. C. Riewe, O. Flament, P. Paillet and J. L. Leray, "The role of electron transport and trapping in MOS total-dose modeling," *IEEE Transactions on Nuclear Science*, vol. 46, pp. 1519 - 1525, 1999.
- [22] G. Massobrio and P. Antognetti, *Semiconductor device modeling with SPICE*, McGraw-Hill, 1998.
- [23] D. Forty, *MOSFET Modeling With SPICE: Principles and Practice*, Prentice Hall, 1997.
- [24] R. M. Kielkowski, *SPICE: Practical Device Modeling*, McGraw-Hill, 1995.
- [25] M. Shur and T. A. Fjeldly, *Silicon and Beyond: Advanced Device Models and Circuit Simulators*, World Scientific Publishing Company Inc., 2000.
- [26] L. W. Ricketts, *Fundamentals of Nuclear Hardening of Electronic Equipment*, John Wiley & Sons Inc., 1972.
- [27] T. R. Oldham, *Ionizing Radiation Effects in Mos Oxides (International Series on Advances in Solid State Electronics and Technology)*, World Scientific Publishing Company Inc., 2000.

- [28] F. Larin, *Radiation Effects in Semiconductor Devices*, Wiley, 1968.
- [29] J. Guldberg, "Electron traps in silicon doped by neutron transmutation," *Journal of Physics D: Applied Physics*, vol. 11, no. 14, p. 2043, 1978.
- [30] E. H. Snow, A. S. Grove and D. J. Fitzgerald, "Effects of Ionizing Radiation on Oxidized Silicon Surfaces and Planar Devices," *Proceedings of the IEEE*, vol. 55, no. 7, pp. 1168 - 1185, 1967.
- [31] D. M. Fleetwood, S. L. Miller, R. A. Reber, P. J. McWhorter, P. S. Winokur, M. R. Shaneyfelt and J. R. Schwank, "New Insights into Radiation-Induced oxide-trap charge through thermally stimulated current measurement and Analysis," *IEEE Transactions on Nuclear Science*, vol. 39, pp. 2192 - 2203, 1992.
- [32] X. J. Chen, H. J. Barnaby, R. D. Schrimpf, D. M. Fleetwood, R. L. Pease, D. G. Platteter and G. W. Dunham, "Nature of interface defect buildup in gated bipolar devices under low dose rate irradiation," *IEEE Transactions on Nuclear Science*, vol. 53, pp. 3649 - 3654, 2006.
- [33] J. A. Felix, D. M. Fleetwood, R. D. Schrimpf, J. G. Hong, G. Lucovsky, J. R. Schwank and M. R. Shaneyfelt, "Total-dose radiation response of hafnium-silicate capacitors," *IEEE Transactions on Nuclear Science*, vol. 49, pp. 3191 - 3196, 2002.
- [34] D. Zupac, K. F. Galloway, P. Khosropour, S. R. Anderson, R. D. Schrimpf and P. Calvel, "Separation of effect of oxide-trapped charge and interface-trapped charge on mobility irradiated power MOSFETs," *IEEE Transactions on Nuclear Science*, vol. 40, pp. 1307 - 1315, 1993.
- [35] F. El-Mamouni, M. Bawedin, E. X. Zhang, R. D. Schrimpf, D. M. Fleetwood and S. Cristoloveanu, "Total dose effects on the performance of irradiated capacitorless MSDRAM cells," *IEEE Transactions on Nuclear Science*, vol. 57, pp. 3054 - 3059, 2010.
- [36] S. C. Witczak, R. D. Schrimpf, K. F. Galloway, D. M. Fleetwood, R. L. Pease, J. M. Puhl, D. M. Schmidt, W. E. Combs and J. S. Suehle, "Accelerated tests for simulating low dose rate gain degradation of Lateral and substrate pnp BJT," *IEEE Transactions on Nuclear Science*, vol. 43, pp. 3151 - 3160, 1996.
- [37] L. Zhou, T. Jackson, E. Brandon and W. West, "Flexible substrate a-Si:H TFTs for space applications," *Device Research Conference: 62nd DRC Conference Digest*, vol. 1, pp. 123 - 124, 2004.
- [38] L. Dong-Mei, W. Zhi-Hua, H. Li-Ying and G. Qui-Jing, "Study of total ionizing dose radiation effects on enclosed gate transistors in a commercial CMOS technology," *Chinese Physics*, vol. 16, no. 12, p. 3760, 2007.
- [39] C. D. Cress, J. J. McMorro, J. T. Robinson, A. L. Friedman and B. J. Landi, "Radiation Effects in Single-Walled Carbon Nanotube Thin-Film-Transistors," *IEEE Transactions on Nuclear Science*, vol.

57, no. 6, pp. 3040 - 3045, 2010.

- [40] P. Paillet, M. Gaillardin, V. Ferlet-Cavrois, A. Torres, O. Faynot, C. Jahan, L. Tosti and S. Cristoloveanu, "Total ionizing dose effects on deca-nanometer fully depleted SOI devices," *IEEE Transactions on Nuclear Science*, vol. 52, no. 6, pp. 2345 - 2352, 2005.
- [41] C. Jagadish and S. Pearton, *Zinc Oxide Bulk, Thin Films and Nanostructures: Processing, Properties and Applications*, Boston: Elsevier, 2006.
- [42] J. R. Schwank, M. R. Shaneyfelt, D. M. Fleetwood, J. A. Felix, P. E. Dodd, P. Paillet and V. Ferlet-Cavrois, "Radiation Effects in MOS Oxides," *IEEE Transactions on Nuclear Science*, vol. 55, no. 4, pp. 1833 - 1853, 2008.
- [43] K. Nomura, T. Kamiya and H. Hosono, "Stability and high-frequency operation of amorphous In-Ga-Zn-O thin-film transistors with various passivation layers," *Thin Solid Films*, vol. 520, pp. 3778 - 3782, 2012.
- [44] D. A. Mourey, M. S. Burberry, D. A. Zhao, Y. V. Li, S. F. Nelson, L. Tutt, T. D. Pawlik, D. H. Levy and T. N. Jackson, "Passivation of ZnO TFTs," *Journal of Society for Information Display*, vol. 18, pp. 753 - 761, 2010.
- [45] O. Volnianska, P. Boguslawski and E. Kaminska, "Ag and N acceptors in ZnO: An ab initio study of acceptor pairing, doping efficiency, and the role of hydrogen," *Phys. Rev. B*, vol. 85, p. 165212, 2012.
- [46] A. A. Sokol, S. A. French, S. T. Bromley, C. Catlow, H. J. van Dam and P. Sherwood, "Point defects in ZnO," *Faraday Discussions*, vol. 134, pp. 267-282, 2007.
- [47] F. Oba, M. Choi, A. Togo and I. Tanaka, "Point defects in ZnO: an approach from first principles," *SCIENCE AND TECHNOLOGY OF ADVANCED MATERIALS*, vol. 12, p. 034302, 2011.
- [48] S. Ramanathan, S. Bandyopadhyay, L. K. Hussey and M. Munoz, "Observation of numerous E2 mode phonon replicas in the room temperature photoluminescence spectra of ZnO nanowires: Evidence of strong deformation potential electron-phonon coupling," *Applied Physics Letters*, vol. 89, p. 143121, 2006.
- [49] S. Singh, D. Nakamura, K. Sakai, T. Okada and M. S. Ramachandra Rao, "Investigation of low-temperature excitonic and defect emission from Ni-doped ZnO nanoneedles and V-doped ZnO nanostructured film," *New Journal of Physics*, vol. 12, p. 023007, 2010.
- [50] T. Kamiya, K. Nomura and H. Hosono, "Origins of High Mobility and Low Operation Voltage of Amorphous Oxide TFTs: Electronic Structure, Electron Transport, Defects and Doping," *Journal of*

Display Technology, vol. 5, pp. 468 - 483, 2009.

- [51] Y. V. Li, K. G. Sun, J. I. Ramirez and T. N. Jackson, "Trilayer ZnO Thin-Film Transistors with In-Situ Al₂O₃ Passivation," *IEEE Electron Device Letters*, vol. 34, pp. 1400 - 1402, 2013.

What opportunities for training and professional development has the project provided?

If the research is not intended to provide training and professional development opportunities or there is nothing significant to report during this reporting period, state "Nothing to Report." Describe opportunities for training and professional development provided to anyone who worked on the project or anyone who was involved in the activities supported by the project. "Training" activities are those in which individuals with advanced professional skills and experience assist others in attaining greater proficiency. Training activities may include, for example, courses or one-on-one work with a mentor. "Professional development" activities result in increased knowledge or skill in one's area of expertise and may include workshops, conferences, seminars, study groups, and individual study. Include participation in conferences, workshops, and seminars not listed under major activities.

There have been several opportunities for training and professional development provided by this project. Faculty and students at Penn State University and AFRL have benefited from professional development and mentorship enabled by this program. The beneficiaries of these activities are listed below.

Faculty supported at PSU includes:

Tom Jackson, Ph.D., Penn State University, Professor of Electrical Engineering

Graduate students supported at PSU include:

Israel Ramirez, Ph.D. student (May 2015)

Ho Him (Raymond) Fok, Ph. D. student (May 2013)

Yuanyuan Li, Ph.D. student (August 2013)

Yi-Chun (Paris) Liu, Ph.D. student (August 2014)

Kaige Sun, Ph.D. student (May 2015)

Myung-Yoon Lee, MS student (May 2015)

Research scientists at AFRL include:

Gregg H. Jessen, Ph.D., AFRL

Kevin Leedy, Ph.D., AFRL

Burhan Bayraktaroglu, Ph.D., AFRL

In addition to professional development of the above students and researchers, there were numerous opportunities to participate in conferences and workshops afforded by the program. Conference and workshop participation is documented in the following section regarding dissemination of results to the communities of interest.

How have the results been disseminated to communities of interest?

If there is nothing significant to report during this reporting period, state "Nothing to Report."

Describe how the results have been disseminated to communities of interest. Include any outreach activities that have been undertaken to reach members of communities who are not usually aware of these research activities, for the purpose of enhancing public understanding and increasing interest in learning and careers in science, technology, and the humanities.

Publications:

J.I. Ramirez, Li Y.V., H. Basantani, D. A. Zhao, T.N. Jackson, K. Leedy, G. H. Jessen, B. Bayraktaroglu, "100 Mrad Gamma-Ray Radiation Tolerance of ZnO Thin Film Transistors." (Submitted to IEEE Transactions on Nuclear Science)

Y. V. Li, K. G. Sun, J. I. Ramirez, and T. N. Jackson, "Low-Voltage Double-Gate ZnO Thin-Film Transistor Circuits," *IEEE Electron Device Letters*, v. 34, no. 7, pp. 891 – 893, 2013.

Presentations:

G. Jessen and T. Jackson, "Radiation-Hard and Self-Healing Substrate-Agnostic Nanocrystalline ZnO Thin Film Electronics," **2014 DTRA Basic Research Technical Review**, (July 2014).

J.I. Ramirez, Y.V. Li, Y. Liu, H. Basantani, K. Leedy, B. Bayraktaroglu, G. H. Jessen, T. N. Jackson, "Radiation Exposure Characteristics of Electrically Biased and Unbiased ZnO TFTs" **NanoTechnology for Defense Conference**, 2014.

G. Jessen and T. Jackson, "Radiation-Hard and Self-Healing Substrate-Agnostic Nanocrystalline ZnO Thin Film Electronics," **2013 DTRA Basic Research Technical Review**, (July 2013).

J.I. Ramirez, Y. Li, K.G. Sun, H. Basantani, T.N. Jackson, "ZnO Thin Film Transistors For Extreme Environment Applications," **IEEE International Semiconductor Device Research Symposium**, 2013.

J.I. Ramirez, Y. Li, K.G. Sun, H. Basantani, T.N. Jackson, "ZnO Thin Film Transistors for Radiation Environment Applications" **SPIE**, 2013.

Y. V. Li, K. G. Sun, J. I. Ramirez, and T. N. Jackson, "Tri-layer PEALD ZnO Thin Film Transistors and Circuits," **2013 Device Research Conference Digest** (June 2013).

Y. Liu, Y. V. Li, J. I. Ramirez, and T. Jackson, "Contact Barrier and Traps in High Performance ZnO TFTs," **2013 Electronic Materials Conference**, (June 2013).

J. I. Ramirez, Y. V. Li, H. Basantani, and T. N. Jackson, "Effects of Gamma-Ray Irradiation and Electrical Stress on ZnO Thin Film Transistors," **2013 Device Research Conference Digest** (June 2013).

G. Jessen and T. Jackson, "Radiation-Hard and Self-Healing Substrate-Agnostic Nanocrystalline ZnO Thin Film Electronics," **2012 DTRA Basic Research Technical Review**, (August 2012).

B. Bayraktaroglu, K. Leedy, Y. V. Li, D. A. Zhao, J. I. Ramirez, H. H. R. Fok, and T. N. Jackson, "Radiation Tolerance and Recovery Characteristics of ZnO Thin-Film Transistors," **GOMACTech-12**, Las Vegas, NV (March 2012).

Y. V. Li, J. I. Ramirez, K. G. Sun, and T. N. Jackson, "Low-Voltage ZnO Double-Gate Thin Film Transistor Circuits," **2012 Device Research Conference** Digest, pp. 239-240 (June 2012).

J. I. Ramirez, Y. V. Li, M. Wallace, and T. N. Jackson, "XRD of ZnO Thin Films by Showerhead Plasma Enhanced Atomic Layer Deposition," **2012 Electronic Materials Conference**, paper K5 (June 2012).

Y.-C. Liu, Y. V. Li, and T. N. Jackson, "Contact Barriers and Traps in PEALD ZnO TFTs," **2012 Electronic Materials Conference**, paper S5 (June 2012).

Y. V. Li, J. I. Ramirez, K. G. Sun, and T. N. Jackson, "Tri-Layer ZnO Thin Film Transistors," **2012 Electronic Materials Conference**, paper FF1 (June 2012).

J. I. Ramirez, Y. V. Li, H. Fok, T. Jackson, K. Leedy, G. Jessen, and B. Bayraktaroglu, "Nanocrystalline ZnO Thin Film Transistors for High Radiation Environment Applications," **2012 NanoTechnology for Defense Conference** (August 2012).

What do you plan to do during the next reporting period to accomplish the goals?

If there are no changes to the agency-approved application or plan for this effort, state "No Change." Describe briefly what you plan to do during the next reporting period to accomplish the goals and objectives.

There are no further actions remaining at the end of the three year period. We suggest future work as originally proposed for Year 4 and Year 5. We also suggest revisiting the advanced materials task and continued materials characterization tasks to include additional sources of radiation.

Year #4 (Optional) (2014)**Task 13: Interactive radiation sensitivity device models**

The scope of this task is to consolidate the physical device models developed in prior years of the program into a comprehensive model that can be used to predict various operational and radiation sensitivity tolerances of thin film electronic devices. The model will be suitable for analyzing the operational characteristics of future device designs without having to fabricate them. In order to gain confidence in the predictive qualities of the device models, we will undertake a verification process under Task 14. This effort will be mostly undertaken by PSU and will be aided by AFRL. The effort will be about 40% of the total effort of the year.

Task 14: Verification of radiation sensitivity models

The object of this task is to use the physical device models developed over the prior 3 years of the proposed program to design device structures that will provide the best operational performance and radiation tolerance. Such designs will then be fabricated, radiation tested and characterized to verify the accuracy of models. This effort will require thin film materials and device fabrication as well as their full characterization at both AFRL and PSU facilities. Multiple iterations of design-fabrication-testing-characterization-verification cycles may be required to gain confidence in the models developed. The effort in this task will be about 55% of the total effort for the year.

Task 15: Annual report

In addition to periodic updates on technical progress (as required), an annual report will be provided at the end of the year that will document the progress for that year. This effort is expected to be about 5% of the total effort of the year.

Year #5 (Optional) (2015)**Task 16: Universal radiation damage models for M-O devices**

The object of this task is to expand the scope of the interactive device models developed in prior years of the project to include the effects of radiation on thin film electro-optical devices. Modifications will be made to the existing models to account for the radiation effects on minority carrier properties, which are important for the operation of optical devices. We will investigate the suitability of such universal radiation sensitivity models for solar-blind UV photodetectors, LEDs, solar cells and lasers. The scope of this task will be limited to uncovering the physical mechanisms responsible for radiation sensitivity of electro-optical devices and identifying the similarities with purely electrical devices. This effort will be mostly undertaken by PSU and will be aided by AFRL. The effort will be about 40% of the total effort of the year.

Task 17: Fabrication, radiation test and analysis of electro-optical devices

This task will address the fabrication, radiation testing and characterization of thin film electro-optical devices to aid in the development of universal thin film device radiation sensitivity models of Task 16. The demonstration device for this effort will be UV photodetectors, which can be fabricated using ZnO-NiO thin film heterojunctions. Other photodetector structures and device types will be considered for this task based on the progress made in developing advanced material deposition techniques in Task 9. The effort in this task will be about 50% of the total effort for the year and will involve fabrication and testing at both AFRL and PSU facilities.

**DISTRIBUTION LIST
DTRA-TR-16-9**

DEPARTMENT OF DEFENSE

DEFENSE THREAT REDUCTION
AGENCY
8725 JOHN J. KINGMAN ROAD
STOP 6201
FORT BELVOIR, VA 22060
ATTN: J. CALKINS

DEFENSE TECHNICAL
INFORMATION CENTER
8725 JOHN J. KINGMAN ROAD,
SUITE 0944
FT. BELVOIR, VA 22060-6201
ATTN: DTIC/OCA

**DEPARTMENT OF DEFENSE
CONTRACTORS**

QUANTERION SOLUTIONS, INC.
1680 TEXAS STREET, SE
KIRTLAND AFB, NM 87117-5669
ATTN: DTRIAC